Title
Magnetic Anisotropy, Damping and Interfacial Spin Transport in Pt/LSMO Bilayers

Permalink
https://escholarship.org/uc/item/4dn1t6vx

Author
Lee, Han Kyu

Publication Date
2017

Peer reviewed|Thesis/dissertation

UNIVERSITY OF CALIFORNIA,
IRVINE

Magnetic Anisotropy, Damping and Interfacial Spin Transport in Pt/LSMO Bilayers

THESIS

submitted in partial satisfaction of the requirements
for the degree of

MASTER OF SCIENCE

in Physics

by

Han Kyu Lee

Thesis Committee:
Professor Ilya N. Krivorotov, Chair
Professor Wilson Ho
Professor Ruqian Wu

2017

TABLE OF CONTENTS

LIST OF FIGURES

ACKNOWLEDGMENTS

Life in past seven years has been quite a journey for me. I want first to express my gratitude to my research advisor, Professor Ilya Krivorotov. Under his generous supports, I learned to appreciate physics research through his intuitions and breadth of knowledge. I want to equally thank Dr. Igor Barsukov for showing me how to do experiments, sharing his perspectives and guiding me on the project that became the basis of this thesis. Without him, this work wouldn't have been possible, and it has been a great privilege to conduct research with him. I am very grateful to Dr. Adrian G. Swartz, Dr. Bongju Kim, and Professor Harold Y. Hwang, our collaborators at Stanford University who provided excellent LSMO films. I want to especially thank for their kind replies to my inquiries related to LSMO.

It is my fortune to join the Krivorotov group surrounded by good colleagues: Yu-Jin Chen, Brian Youngblood, Chris Safranski, Alejandro Jara, Andrew Smith, Liu Yang, Jieyi Zhang, Jenru Chen, and Chengcen Sha. They made the lab an exciting place to do research. I especially appreciate Yu-Jin who had patiently clarified all my basic questions and shared great knowledge on ST-FMR measurements.

I am also grateful to Professor Wilson Ho and Professor Ruqian Wu for serving the thesis committee. I want to thank talented Wilson Ho group members who I had a privilege to interact especially with Chi-lun Jiang, Shaowei Li, Freddy Toledo, and Dr. Haigang Zhang for all their help.

Finally, my deepest thanks go to my parents Hyung Hwan and Myung Soon, for all their unconditional supports, and to my wife Gyo Sun, I become a better man by her encouragements and cheerfulness.

ABSTRACT OF THE THESIS

Magnetic Anisotropy, Damping and Interfacial Spin Transport in Pt/LSMO Bilayers

By

Han Kyu Lee

Master of Science in Physics

University of California, Irvine, 2017

Professor Ilya N. Krivorotov, Chair

In this thesis, I describe ferromagnetic resonance measurements of magnetic anisotropy and damping in epitaxial $La_{0.7}Sr_{0.3}MnO_3$ (LSMO) and Pt capped LSMO thin films on $SrTiO_3$ (001) substrates. The measurements reveal significant negative perpendicular magnetic anisotropy and a weaker uniaxial in-plane anisotropy that both are unaffected by the Pt cap. The Gilbert damping of the bare LSMO films is found to be low $\alpha = 1.9(1) \times 10^{-3}$, and two-magnon scattering is determined to be significant and strongly anisotropic in the plane of the film. The Pt cap increases the damping by 50% due to spin pumping, which is also directly detected via inverse spin Hall effect in Pt. This work demonstrates efficient spin transport across the Pt/LSMO interface.

Chapter 1

Introduction

Spin transport across an interface between nonmagnetic metal (NM) and ferromagnet (FM) by spin Hall effect (SHE) [1] and spin pumping [2, 3, 4] is central to manipulation of magnetization dynamics driven by pure spin currents. To date, significant focus has been set on FM/NM heterostructures comprising 3d materials [5, 6, 7, 8] with a recent extension to yttrium iron garnet (YIG) [9, 10, 11]. While these systems provided great insights about underlying physics of SHE and the spin pumping [5, 11], transition metal ferromagnets exhibit high saturation magnetization and large magnetic damping that result in high critical current densities in SHE-based magnetic memories [6] and spin torque oscillators [12, 13]. For enriching these applications, identification of new material platforms for the efficient generation, transmission, and conversion of spin currents will be greatly beneficial.

In this context, perovskite manganite $La_{0.7}Sr_{0.3}MnO_3$ (LSMO) is an attractive ferromagnet because it has low saturation magnetization, and expected to show low magnetic damping owing to its half-metallic nature [14]. In this thesis, I present ferromagnetic resonance measurements of magnetic anisotropy and damping in epitaxial LSMO films grown on $SrTiO_3$ (001) (STO) substrates with and without Pt cap. We observe low magnetic damping and efficient interfacial spin transport in this system, which makes Pt/LSM bilayer a promising candidate

for spintronic devices utilizing pure spin currents.

In Chapter 2, a brief background about $La_{0.7}Sr_{0.3}MnO_3$ (LSMO), review of fundamental concepts in magnetism, basics of ferromagnetic resonance, and the experimental setup will be discussed.

In Chapter 3, experimental results from ferromagnetic resonance measurements on a single layer LSMO thin film and Pt/LSMO bilayer are presented. First, I describe an observation of large negative perpendicular magnetic anisotropy and a weaker uniaxial in-plane anisotropy in the system. Magnetic damping shows the low Gilbert damping and significant contribution of two-magnon scattering in this system. Due to spin pumping in the Pt/LSMO bilayer, enhancement of the damping and detection of inverse spin Hall effect are presented.

The last chapter is the conclusions and perspectives.

Chapter 2

Background

In this chapter, a brief background about $La_{0.7}Sr_{0.3}MnO_3$ followed by fundamental concepts of magnetic anisotropy and magnetic dynamics are introduced. Afterward, basics of ferromagnetic resonance (FMR), the experimental setup based on a coplanar waveguide, and a review of FMR analysis will be presented.

2.1 $La_{0.7}Sr_{0.3}MnO_3$ (LSMO)

The crystal structure of a perovskite manganite $La_{0.7}Sr_{0.3}MnO_3$ (LSMO) is shown in Fig. 2.1. From the generic form ABO_3 of a perovskite structure, lanthanum (La) or substitutionally doped (30%) strontium (Sr) atoms occupies the "A" sites and form a cubic unit cell. Manganese (Mn) atoms occupy at the "B" site surrounded by oxygen atoms and form a MnO_6 octahedron [15]. This system exhibits rich interactions between the charge, spin, orbital, and lattice degrees of freedom leading to complex electronic and magnetic phase diagrams, e.g. a doping-dependent metal-insulator transition, paramagnetism, ferromagnetism, and antiferromagnetism [15].
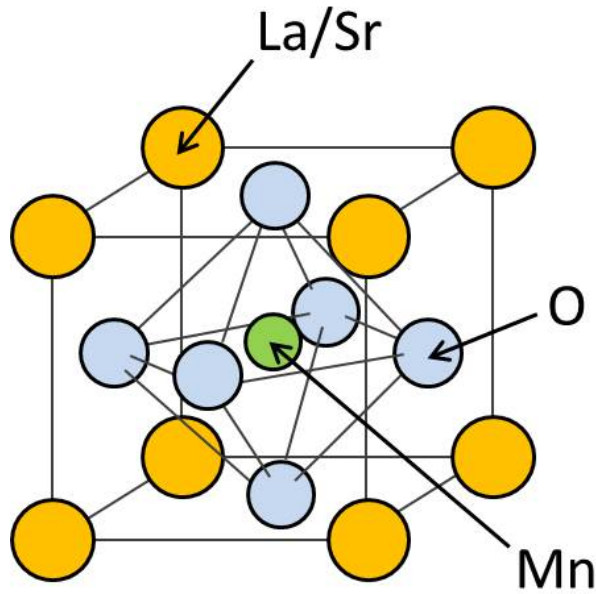
Figure 2.1: Crystal structure of $La_{0.7}Sr_{0.3}MnO_3$ (LSMO) which has perovskite-based structure having a general form ABO_3. In LSMO, lanthanum (La) or substitutionally doped (30%) strontium (Sr) atoms occupies the "A" site and the manganese (Mn) atoms occupies the "B" sites surrounded by oxygen atoms forming a MnO_6 octahedron.

In the emerging field of spintronics, LSMO is perhaps best known for its half-metallic band structure having 100% spin polarization at the Fermi surface, for more details see Ref. [15] and the references therein. The half-metallicity makes LSMO an attractive candidate as spin-filtering material in magnetic tunnel junctions (MTJs) for generation of spin-polarized currents. For example, tunneling magnetoresistance ratio of 1800% at 4 K is demonstrated in Ref. [16] due to spin polarization of at least 95% in LSMO electrodes. In addition, LSMO has high Curie temperature (T_C) above room temperature and low saturation magnetization [17]. In fact, the half-metallic nature is expected to result in low magnetic damping [14, 18]. All these properties are favorable for reducing critical current density in spin torque oscillators having LSMO as the active layer, in which the manipulation of magnetization dynamics occur. Lastly, this oxide system can be grown epitaxially with atomically sharp interfaces [19, 20], holding a great potential as a tunable platform to enable interfacial engineering [21].

2.2 Magnetic Anisotropy

At a temperature below the Curie temperature T_C, ferromagnetic materials exhibit spontaneous ordering that all its magnetic moments $\vec{\mu}$ align in the same direction by the exchange interaction [22, 23]. These moments arises from spin- and orbital angular momentum of electrons and the total magnetic moments over the volume V is called magnetization $\vec{M} = \left(\sum \vec{\mu}_i\right)/V$ of a sample [22, 23]. The orientation of magnetization $\vec{M}$ within a sample has directional dependence called magnetic anisotropy and described by magnetic anisotropy energy (MAE). The magnetization tends to align in the direction, called easy axis, that minimizes the energy and hinders to align in the direction, called hard axis, which maximizes the energy. Among several contributions of magnetic anisotropy, Zeeman energy, magnetocrystalline anisotropy, and uniaxial magnetic anisotropy are the most important contributions in this thesis. Discussions of magnetoelastic (induced by stress) and exchange anisotropy (induced from a neighboring antiferromagnet) that have no contributions are omitted.

The spherical coordinate system is used throughout the thesis. The azimuthal angles ϕ and polar angles θ for magnetization are referenced to the [100] direction in the plane of the magnetic thin film and the [001] direction, out-of-plane of the film, respectively. When the magnitude of external magnetic field H (or sometimes denoted as H_ext) is above saturation field H_sat ($H > H_\mathrm{sat}$, or called a saturated regime), the equilibrium direction of the magnetization is aligned parallel to the external field direction. Throughout the thesis, the saturated regime is assumed, and the polar and azimuthal angles are used to represent both the magnetization and the external magnetic field interchangeably otherwise noted.

Zeeman Energy

Zeeman energy is a potential energy density of magnetization under the external magnetic field $\vec{H}$ and the energy minimum occurs when the magnetization is parallel to the external

field.

$$F_{\text{Zeeman}} = -\vec{M} \cdot \vec{H} \tag{2.1}$$

Magnetocrystalline Anisotropy

Magnetocrystalline anisotropy (MCA) arises from spin-orbit interaction that couples the magnetic moment of the electron with the crystal lattice [22, 23, 24]. As a consequence the magnetization prefers to align along well-defined crystallographic axes. In practice, the free energy density of magnetocrystalline anisotropy F_{mc} is phenomenologically derived based on power series expansion of direction cosines α_i of the magnetization $\vec{M} = M_s(\alpha_x, \alpha_y, \alpha_z)$ with respect to the crystallographic axes [22, 23, 24]. M_s is the saturation magnetization. The crystal system detemines the nonzero terms in the expansion and only even powers of the cosines are allowed when symmetry requires that $F_{\text{mc}}(\alpha_i) = F_{\text{mc}}(-\alpha_i)$, i.e. if 180° rotation is identical in the α_i direction.

In a cubic crystal, the lowest order term in the energy density is [24]:

$$\begin{aligned}
F_{\text{mc}} &= K_{mc}\left(\alpha_x^2\alpha_y^2 + \alpha_y^2\alpha_z^2 + \alpha_z^2\alpha_x^2\right) \\
&= K_{\text{mc}}\sin^2\theta - \frac{1}{8}K_{\text{mc}}\left(7 + \cos 4\phi\right)\sin^4\theta \\
&= \frac{1}{2}M_s\left(\frac{2K_{\text{mc}}}{M_s}\right)\sin^2\theta - \frac{1}{16}M_s\left(\frac{2K_{\text{mc}}}{M_s}\right)(7 + \cos 4\phi)\sin^4\theta \\
&= \frac{1}{2}M_sH_{\text{mc}}\sin^2\theta - \frac{1}{16}M_sH_{\text{mc}}(7 + \cos 4\phi)\sin^4\theta,
\end{aligned} \tag{2.2}$$

where K_{mc} is first order anisotropy constant which has *four-fold* symmetry. The corresponding anisotropy field is $H_{\text{mc}} = 2K_{\text{mc}}/M_s$, which is a useful quantity for comparing the strength of magnetic anisotropies in the system. A positive $K_{\text{mc}} > 0$ results easy axes and hard axes along the ⟨100⟩ and ⟨111⟩ directions, respectively. The projection of hard axes ⟨111⟩ on to the plane of the film results ⟨110⟩ as hard axes within the plane. A contribution from second

6

order anisotropy could be considered but not shown here.

Lastly, the first term in the last line of Eqn. (2.2) can be expanded as $\frac{1}{2}M_sH_{\mathrm{mc}}-\frac{1}{2}M_sH_{\mathrm{mc}}\cos^2\theta$ but the first term of the expanded expression can be neglected because $\frac{1}{2}M_sH_{\mathrm{mc}}$ has no angular dependence. The final expression of the energy density is

$$F_{\mathrm{mc}} = -\frac{1}{2}M_{\mathrm{s}}H_{\mathrm{mc}}\cos^2\theta - \frac{1}{16}M_{\mathrm{s}}H_{\mathrm{mc}}(7+\cos 4\phi)\sin^4\theta, \qquad (2.3)$$

Shape Anisotropy: Demagnetization Field

A finite volume of magnetic material produces magnetic charges at the surface as a solution to the boundary problem in magnetostatics [23]. The magnetic surface charges or surface poles is a source of a physically observable magnetic field called demagnetizing field H_{demag}. The demagnetizing field, as the name suggest, acts in opposition to the magnetization $\vec{M}$ at inside the volume and continues as a dipolar stray field at the outside. The demagnetizing field depends upon the shape of the volume because the surface poles distribution varies as the magnetization orientation changes and give rise to the shape anisotropy.

In general, calculation of demagnetizing field is quite challenging and often requires numerical computation except for few highly symmetric geometries, e.g. uniformly magnetized sphere and ellipsoids [22, 25]. In thin films, edges of the plane can be approximated as semi-infinitely separated and corresponding surface poles can be assumed to be vanishingly small. The surface charges occur only in the direction normal to the film plane, and the shape anisotropy is described by [22, 23, 24]

$$F_{\mathrm{shape}} = \frac{1}{2}\,4\pi M_s^2\cos^2\theta, \qquad (2.4)$$

where M_s is the saturation magnetization and θ is the polar angle. The shape anisotropy always favors the magnetization to lie within the plane of the film, i.e. the energy minimum

7

occurs at $\theta = 90°$.

Perpendicular Magnetic Anisotropy

As thickness of thin films becomes smaller, the role of surface becomes significant and the preferential direction of the magnetization can change from the commonly observed in-plane orientation (due to shape anisotropy) to the out-of-plane direction. This originates from considerably different magnetic anisotropy at the surface or interface compared to the bulk of the film due to having lowered symmetry and surface oxidation at the surface/interface [23, 26]. The free energy density of perpendicular magnetic anisotropy (PMA) $F_\perp$ is described by [23, 24, 26],

$$
\begin{aligned}
F_\perp &= -\frac{2K_\mathrm{s}}{t_\mathrm{film}} \cos^2 \theta \\
&= -K_\perp \cos^2 \theta \\
&= -\frac{1}{2} M_s \left(\frac{2K_\perp}{M_s} \right) \cos^2 \theta,
\end{aligned}
\tag{2.5}
$$

where $K_\perp$ is the PMA constant which has *two-fold* symmetry with respect to out-of-plane direction. The $K_\perp$ can be both positive or negative depending on the thickness of the film t_film. For $K_\perp > 0$, the easy-axis is along the out-of-plane direction, $\theta = 0°$. In the literature, e.g. Ref. [26], the PMA constant is denoted by K_s with a prefactor 2 to account contribution from both surfaces, e.g. top and bottom of the film. The accurate determination of K_s requires thickness dependent measurements, which I did not performed in this work and I lumped it as $K_\perp = 2K_\mathrm{s}/t_\mathrm{film}$.

Lastly, the anisotropic constants K_i or anisotropic fields H_i are often grouped together by the symmetry of the magnetic anisotropy. For example, the shape anisotropy and PMA have *two-fold* symmetry with respect to the out-of-plane direction. These contributions are often reported in the literature as the effective out-of-plane magnetic anisotropy with the

corresponding anisotropy field H_{eff},

$$H_{\text{eff}} = 4\pi M_{\text{s}} - 2K_{\perp}/M_{\text{s}} \qquad (2.6)$$

Uniaxial Magnetic Anisotropy

Additional uniaxial anisotropy could be presented within the plane of the sample. It could arise from dipole interaction between small areas ($\sim 10\,\text{nm}$) of the sample and local variations of the magnetic parameters that a global magnetic anisotropy can be resulted [27]. The free energy density of the uniaxial anisotropy can be described by [24]

$$F_{\text{uni}} = -\frac{1}{2}M_{\text{s}}H_{\text{uni}}\cos^2(\phi - \phi_{\text{uni}})\sin^2\theta, \qquad (2.7)$$

where ϕ_{uni} is the angle between the easy axis of UMA with respect to the [100] crystallographic axis for the positive $H_{\text{uni}} > 0$.

2.3 Magnetization Dynamics

In previous chapters, static magnetic properties have been considered, where equilibrium magnetization is aligned to a time-independent effective field $\vec{H}_{\text{eff}}$. The effective magnetic field consists of the applied external field $\vec{H}_{\text{ext}}$, shape anisotropy (demagnetization) field $\vec{H}_{\text{demag}}$, PMA field $\vec{H}_{\perp}$, uniaxial anisotropy (dipolar) field $\vec{H}_{\text{uni}}$, and magnetocrystalline anisotropy field $\vec{H}_{\text{mc}}$. When the magnetization is driven out of its equilibrium, e.g. via ferromagnetic resonance, the magnetization process around $\vec{H}_{\text{eff}}$ and the motion is described by Landau-Lifshitz-Gilbert (LLG) equation [24, 28]:

$$\frac{d\vec{M}}{dt} = \gamma\vec{M} \times \vec{H}_{\text{eff}} + \frac{\alpha}{M_{\text{s}}}\vec{M} \times \frac{d\vec{M}}{dt}, \qquad (2.8)$$

where γ and α are the gyromagnetic ratio and Gilbert damping constant, respectively. The magnetization $\vec{M}$ is treated as uniform (within macrospin approximation) with a constant magnitude M_s [24, 28]. The first term describes the precession of magnetization due to torque applied by the effective magnetic field $\vec{H}_{eff}$. The second term describes magnetization relaxation or damping, characterized by the Gilbert constant α [24, 28]. In the absence of damping, the magnetization precesses indefinitely about the effective field at a constant precession cone angle. The damping causes the precession angle to decrease and the magnetization returns in direction of the effective field at its equilibrium. The general trajectory of the magnetization described by Eqn. (2.8) is a spiral towards the effective field.

2.4   Ferromagnetic Resonance

Ferromagnetic resonance (FMR) is a standard technique for probing magnetization dynamics in ferromagnetic materials. In FMR, the magnetization of the ferromagnet is resonantly excited by RF magnetic field $\vec{H}_{RF}$, which oscillates at microwave frequency f_{drive} and applied in the direction transverse to the external magnetic field $\vec{H}_{ext}$. The sample absorbs the microwave power at the resonance when the drive frequency f_{drive} coincides with the resonance frequency f_r of the magnetization. The magnetic anisotropy and damping in the system can be extracted by analyzing the frequency and angular dependent FMR spectra.

There exist several schemes to perform the FMR measurements, e.g. generally cavity-based setup and coplanar waveguide (CPW) based methods. In this work, CPW-based FMR setup is employed, and a magnetic sample is placed closely onto a CPW board [29]. A microwave diode and a lock-in amplifier are used as a detection unit operated under a field modulation scheme [30].

2.4.1 Coplanar Waveguide (CPW)

A coplanar waveguide consists of a coplanar layer of three conductors with thickness d, arranged in ground-signal-ground (GSG) configuration, on a dielectric substrate with thickness h. The microwave signal is applied to the center strip conductor, called signal line, while two outer conductors are ground planes, spaced b away from the signal line. A variant of CPW, called grounded CPW (GCPW) or conductor-backed CPW (CBCPW) is used in this work, which has an additional bottom ground plane connected to top ground planes through conducting bridges called vias, see Fig 2.2(a).

The electromagnetic (EM) wave propagation in GCPW operates in quasi-transverse electromagnetic (TEM) mode [31]. The sketch of static EM field lines in GCPW are shown in Fig. 2.2(b). Although the direction of microwave magnetic field H_{RF} lies within the plane, it has a nonzero component in the out-of-plane direction especially near the edges of the signal line. The strength H_{RF} is the most dominant in the area above the signal line than above the ground planes. The coplanar ground conductors carry much less current density than the signal line because the ground current is separated by three ground conductors and have broader cross-sectional areas. Therefore the dominant area of FMR absorption occurs above the signal line.

I outline few notes on the design of CPW based on Ref. [31]. Any CPW variations, in general, the EM wave resides in both air, and dielectric substrate and the difference of phase velocity in each region causes unwanted longitudinal EM components, parallel to the axis of the signal line. In GCPW, this problem can be alleviated by allowing GSG coplanar layer to have stronger coupling between GSG interfaces, e.g. more E-field in the air than in the dielectric, to reduce inhomogeneity in the region of the wave propagation effectively. The vias in GCPW are employed to help proper grounding. Also, engineering the vias placements are essential for suppressing unwanted parasitic wave modes and achieving the desired impedance, usually $50\,\Omega$ for microwave devices, or loss characteristic of GCPW. For example,

11
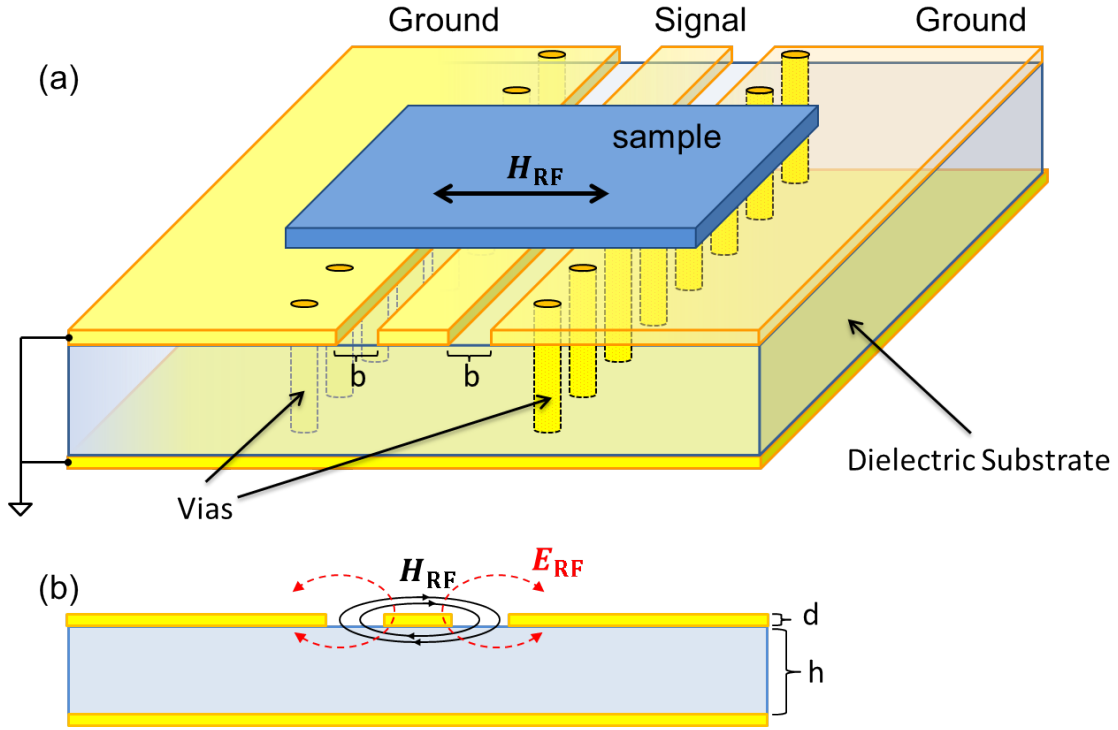
Figure 2.2: A cross-sectional geometry of a grounded coplanar waveguide (CPW) (a) Top coplanar layer consist of ground-signal-ground (GSG) planes separated by spacing b. The bottom ground plane is separated from the top GSG layer by a dielectric substrate with thickness h. Conducting bridges called vias electrical connect the upper and lower ground planes. In typical CPW-FMR measurements, a magnetic film is placed face downward closely onto the surface of GSG layer and driving microwave magnetic field H_{RF} is generated in the direction perpendicular to the axis of the signal line. (b) Sketch of static electric and magnetic field distributions of quasi-TEM modes in the CPW.

a properly designed GCPW can achieve a constant microwave power loss over a wide range of frequencies up to 50 GHz by minimizing frequency dependence in radiation loss [32]. In the rest of chapters in the thesis, I will refer GCPW as simply CPW.

2.4.2   CPW-FMR Experimental Setup

The ferromagnetic resonance measurements are performed by CPW-based setup (CPW-FMR) as shown in Fig. 2.3. A continuous microwave signal is applied to the CPW and the transmitted signal, via microwave diode, is measured by a lock-in amplifier referenced at
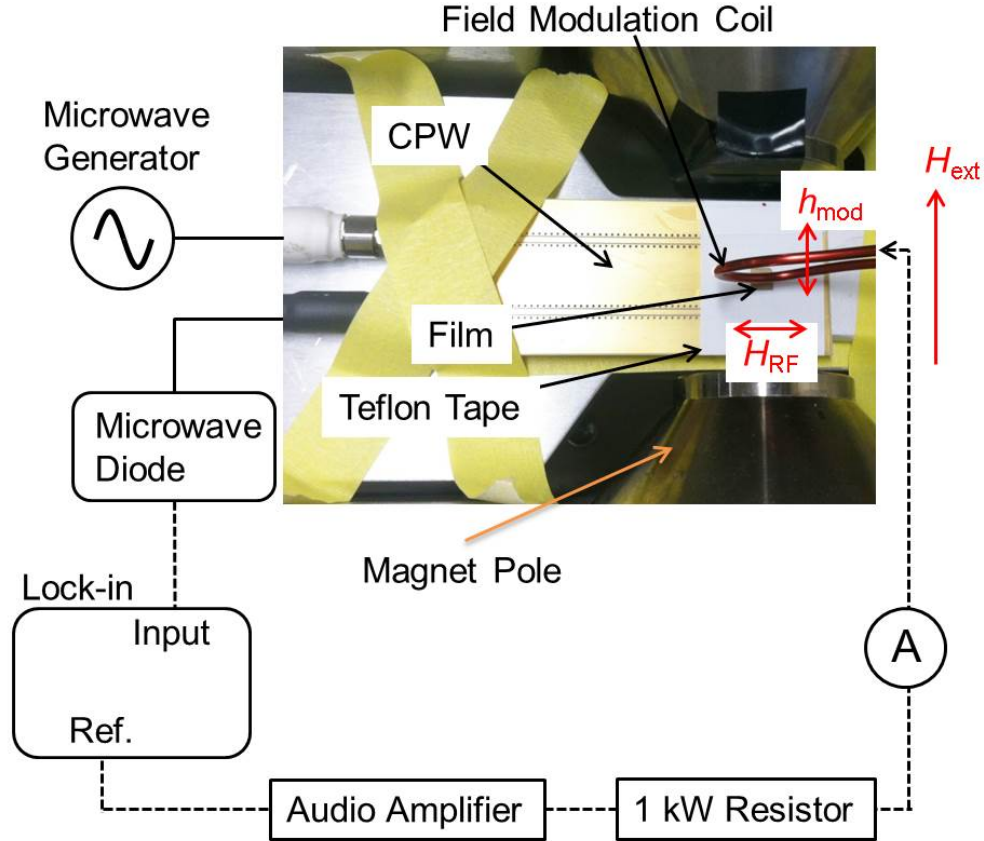
Figure 2.3: A Schematic of CPW based ferromagnetic resonance (FMR) setup. A magnetic film is placed onto the CPW separated by a single layer of Teflon tape. The CPW board is designed to have a "U" shaped transmission line, and two SMA connectors are connected to microwave generator and microwave diode. Microwave current is sent to one of the RF connector which generates a driving microwave magnetic field, H_{RF}, in the direction perpendicular to signal line axis. The signal line is aligned collinearly with the static external magnetic field H_{ext} which is directed in-plane of the film and makes H_{RF} transverse direction to the external field. A transmitted microwave current through the CPW that arrives at microwave diode gets converted into DC voltage and measured by a lock-in amplifier. The lock-in amplifier is referenced to the modulation frequency of AC current in a field modulation coil. The modulation coil is suspended above the film, and the AC current passing through the coil generates an AC Oersted field, h_{mod}. In the schematics, the straight and dotted lines represent microwave and DC cables, respectively.

a frequency which modulates the external magnetic field. The biggest advantage of using CPW-FMR setup is the broadband capability (0.1 - 40 GHz) having access to both frequency and field-domain measurements with high resolution [29].

The transmission line (GSG coplanar layer) of CPW employed in this work is designed as "U" shape geometry, and a complete CPW unit has two 2.92mm connectors (Southwest, End launch connectors model 1092-03A-6) manually installed. The CPW unit is placed in between the pole gap of an electromagnet (GMW, Model 5403), which provides in-plane external magnetic field. Alignment of the field direction as collinear to the straight section of the transmission line where a sample will be mounted is necessary, see a picture in Fig. 2.3 taken from above of the setup. I wrapped the CPW with a single layer of thread seal tape (also known Teflon tape) of approximately $90\,\mu$m thickness, which electrically isolates the sample from CPW conductors. The Teflon tape is slightly stretched to avoid any wrinkles and secured by scotch tape at the back or at near the edge of the CPW. Two 2.92mm connectors are connected to a microwave generator and a microwave diode detector (Keysight, formerly Agilent, Model 8474B, 0.01 - $18\,$GHz) by RF cables, which is represented as straight lines in Fig. 2.3. The order of this equipment to the connectors does not matter because CPW is symmetrical and the same model 2.92mm connectors are manufactured identically. Microwave (RF) signal is sent to the CPW from the microwave generator and propagates through the CPW with the generation of microwave magnetic field H_{RF}, see Fig 2.2(b). When the magnetic film is subjected to H_{RF}, the precession of magnetization is excited by absorbing microwave power and decreases the transmitted microwave signal. The transmitted signal arriving at the input of the microwave diode is converted to DC voltage at the output. The DC voltage of microwave diode output is in general sensitive to input microwave power and frequency that nonlinear background signals can arise in addition to any parasitic signals that both are independent of magnetic properties of the film. To increase the signal-to-noise ratio (SNR), suppression of any unwanted nonmagnetic signals is critical. The suppression of nonmagnetic signal is achieved by employing field modulation scheme [30] using a field

14

modulation coil suspended above the magnetic film and CPW as shown in Fig. 2.3.

The field modulation coil is made by bending copper wires in small loops. It delivers modulation field h_{mod} of few Oersted around the loop by AC current flowing through the coil, typically 1-4 A_{rms} modulated at 300-2000 Hz in our setup. Above the film, the coil is oriented to make the modulation field collinear with the external magnetic field. The AC current is injected by the audio amplifier (Behringer, Model Europower EP4000). The input AC voltage to the audio amplifier is controlled by the reference output of the lock-in amplifier and output AC current from the amplifier is monitor by an ammeter. A 1 kW (4.7 Ω) resistor (TE Connectivity, Model CJT10004R7JJ) is connected in series between the output of the audio amplifier and the modulation coil to match the load impedance and take the most of the joule heating to avoid overheating of the modulation coil. The 1 kW resistor gets quite warm typically around 3.5 A_{rms} and any objects nearby the resistor should be avoided all times.

Setup for Angular Dependent FMR Measurements

For identification of several contributions in the magnetic anisotropy and magnetic damping, angular dependent FMR measurement is required as a function of an angle ϕ between external field and in-plane crystallographic direction of the film. At each different angles, the film should be placed ideally at the same location on the CPW and between the electromagnet pole gap. While engineering a mechanical and ideally automated apparatus to place the thin film, usually deposited on a small and thin substrate, onto the CPW is an interesting challenge, it can become expensive and perhaps cumbersome to make. Instead, I achieved this by attaching the film to a transparency paper printed with a polar graph. The angular dependent measurements are carried out by rotating the transparency paper together with film as a whole unit using a tweezer until the angle, and the ideal position of the film is achieved.
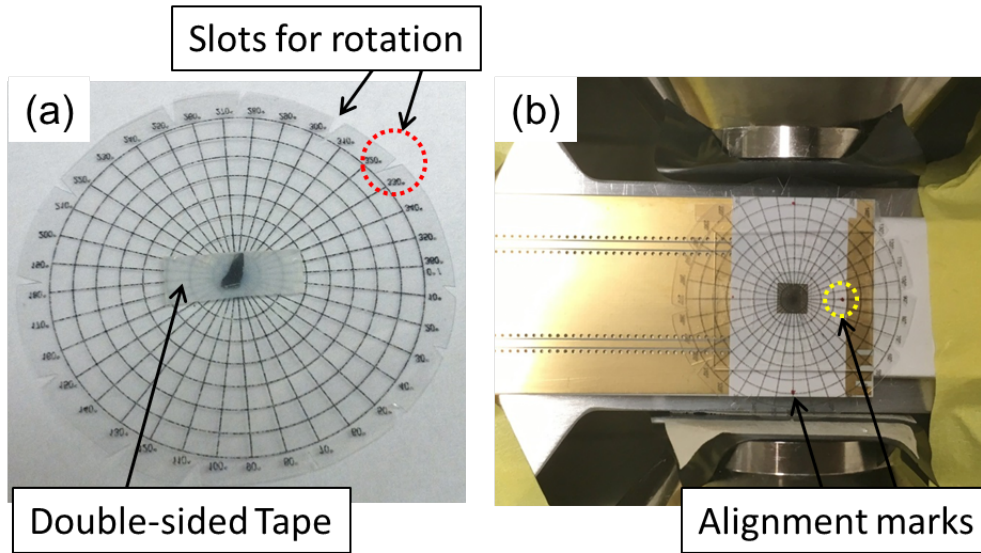
Figure 2.4: A setup for angular dependent FMR measurements. (a) The back of LSMO/STO sample is attached to a transparency paper printed with a polar graph via double-sided tape. The image shows LSMO film facing up. The transparency paper is cut into a small circle with "V" shaped slots around its circumference. (b) The polar graph with the sample attached is placed onto the CPW with film facing down. Four small red dots are previously marked on the Teflon tape are used as alignment marks. As the polar graph is rotated or moved by tweezers using the slots as anchoring, the polar graph, and the film as one unit typically moves away from a center position. The film is brought back to the center position for each target angle using the alignment marks and lines in the polar graph as a guide to the eye. A thin glass slide is diced into a small piece and added to the back of the polar graph transparency paper via double-sided tape as a weight.

The image in Fig. 2.4(a) shows LSMO film facing up on a polar graph that has labels in every 10 degrees. The back of STO substrate, having LSMO film at its front, is attached to a polar graph printed on a transparency paper via double-sided tape. Afterward, the transparency paper is cut into a small circle enough to fit between the pole gap, and a multiple numbers of "V" shaped slots are created around the circumference edge. Figure 2.4(b) shows a final installment of the polar graph with the film onto the CPW with the LSMO film facing down. The four small red dots are previously marked on the Teflon tape as alignment marks. By inserting the tweezer tip into the "V" slots and the film is rotated to a target angle. As the polar graph is rotated, the polar graph and the film as one unit typically moves away from the ideal center position. The film can be brought back to the center position using the alignment marks and lines in the polar graph as a guide to the eye. The validity of this method is checked by measuring FMR resonance at a random angle, subsequently messing up the angles and the position of the film and then remeasuring the resonance at the same angle. A precise rotation of film can be done by at least $5°$ resolution within $\pm 2°$ error.

2.4.3 Analysis of FMR Data

In FMR, the magnetization of the ferromagnet is resonantly excited by microwave magnetic field at driving frequency f_{drive}. In this work, the FMR spectrum is taken in the field-domain that the magnitude of magnetic field is swept at a constant drive frequency f_{drive}. As the magnitude of magnetic field H is swept, the corresponding resonance frequency f_{r} changes. The resonance condition occurs when the drive frequency f_{drive} coincides with the resonance frequency f_{r} and the microwave power is absorbed by the sample. The resonance signal $V(H)$ is in general described by the sum of symmetric and antisymmetric Lorentzian $L_s(H) = \frac{1}{1+((H-H_{\text{r}})/\Delta H)^2}$ and $L_a(H) = \frac{(H-H_{\text{r}})/\Delta H}{1+((H-H_{\text{r}})/\Delta H)^2}$, respectively [30, 33]:

$$V(H) = S\, L_s(H) + A\, L_a(H),\tag{2.9}$$

where H denotes the magnitude of the external magnetic field, ΔH is the FMR linewidth, S and A are the amplitude of symmetric and antisymmetric Lorentzian, respectively. The antisymmetric Lorentzian $L_a(H)$ arises when nonzero phase difference between the microwave electric and magnetic field occurs due to the losses of microwave propagating inside the CPW and the ferromagnetic material [33].

In this work, I measured FMR absorption in the field domain under the field modulation scheme. When the modulation field h_{mod} is small compared to the FMR linewidth ΔH, the voltage signal measured by the lock-in amplifier is proportional to the first derivative of the $V(H)$ with respect to the modulated external magnetic field [30]:

$$V_{\mathrm{mod}}(H) \propto S\,\frac{dL_s(H)}{dH} + A\,\frac{L_a(H)}{dH}, \tag{2.10}$$

Figure 2.5 shows a typical field-modulated FMR spectrum of LSMO thin film on STO(001) substrate. The data, black open circles, is well fitted (green straight line) to the Eqn. (2.10) by a single FMR absorption profile. The symmetric and antisymmetric components of Lorentzian from the fit are shown in Fig. 2.5(a) with the offset for clarity. I note that in the field-modulated FMR spectrum, the symmetric (antisymmetric) Lorentzian appears as antisymmetric (symmetric) profile with respect to the resonance field H_r, respectively. The resonance field H_r and half width at half maximum FMR linewidth ΔH are extracted from the fit as shown in Fig. 2.5(b). The relationship between microwave frequency and resonance field called FMR dispersion gives information about static magnetic properties, e.g. the spectroscopic splitting factor g and magnetic anisotropy fields, latter may depend on the magnetization orientation with respect to the crystallographic direction. The linewidth ΔH is directly related to the magnetic damping.
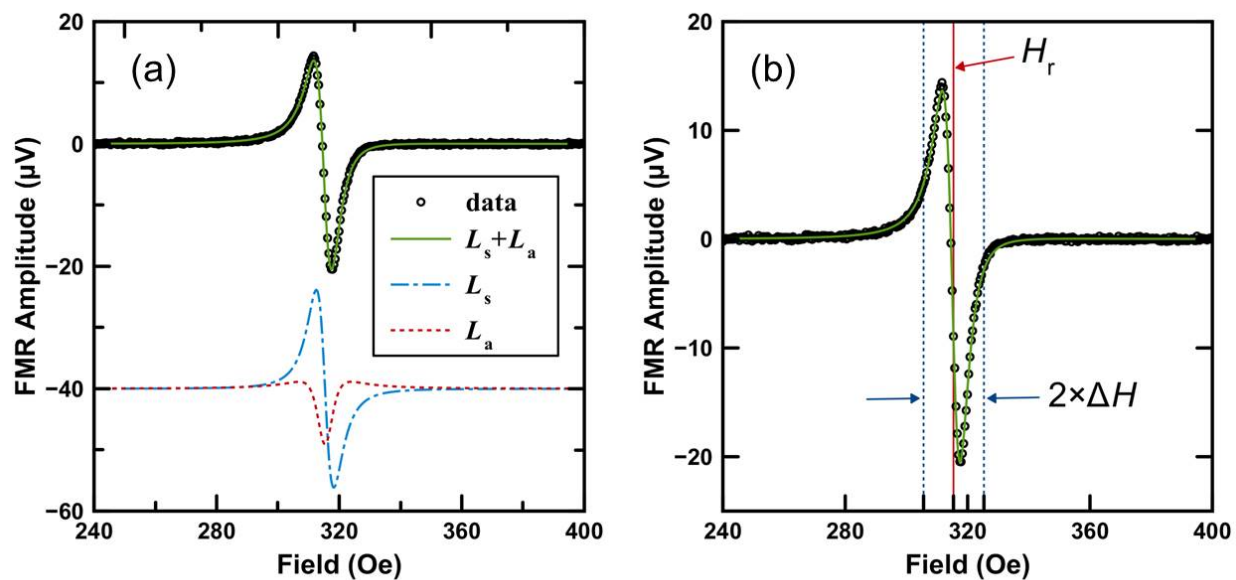
Figure 2.5: An example of field-modulated FMR spectrum of LSMO(30 nm) measured at 4 GHz frequency in the field domain. (a) The data, black open circles, shows a single absorption profile and well fitted, green straight line, to the Eqn. (2.10). The symmetric Lorentzian L_s (blue, dotted-dash line) and antisymmetric L_a (red, dotted line) are shown with offset for clarity. (b) The resonance field $H_r = 315.4$ Oe and FMR linewidth $\Delta H = 4.9$ Oe are extracted from the fit.

Resonance Condition

Under resonant excitation, the torque generated by the microwave field balances the damping term and the remaining equation of motion is that of Eqn. (2.8) without the second term, forcing a precession at the resonance frequency of the system. The resonance condition is formulated by the Smit and Beljers in 1955, also by Suhl at the same time [24, 28]:

$$\left(\frac{2\pi f}{\gamma}\right)^2 = \frac{1}{M^2 \sin^2\theta}\left[\frac{\partial^2 F}{\partial\theta^2}\frac{\partial^2 F}{\partial\phi^2} - \left(\frac{\partial^2 F}{\partial\theta\partial\phi}\right)^2\right],\qquad(2.11)$$

where f is the resonance frequency, $\gamma = g\mu_{\mathrm{B}}/\hbar$ is the gyromagnetic ratio, g is the spectroscopic splitting factor [28], and μ_{B} is the Bohr magneton. The partial derivatives in Eqn. (2.11) are evaluated at the equilibrium angles θ_{eq} and ϕ_{eq}, which are obtained from minimizing the total free energy density F of the system, see Ref. [24] for more details.

Simulation of FMR Dispersion

From the FMR experiment, the resonance field H_r at different microwave frequency f (f vs H data or FMR dispersion) are collected and compared to the Eqn. (2.11) to determine magnetic anisotropies in the system. In this work, calculation of the resonance frequency is carried out by writing a Python script as a function of the magnetic field and in-plane angle of the field ϕ referenced to the crystal axis [100]. The initial value of fitting parameters g, H_1, H_{mc}, H_{uni} and ϕ_{uni} are first assigned and carried out the calculation to simulate FMR dispersion; I refer it as simulation dispersion. Subsequently, the simulation dispersion is compared to the experimental FMR dispersion, and the value of fitting parameters are adjusted until the best simulation result to the data is achieved. To increase the accuracy, a set of FMR dispersion data is taken at different angles, e.g. $\phi = 0, 40, 90°$ in this work, and all compared simultaneously to a set of simulation dispersions at the same angles, generated while using the identical value of the fitting parameters. Furthermore, angular dependent FMR data are

collected at few different microwave frequencies. Following the procedure outlined for the simulation of FMR dispersion, the angular dependent FMR can be simulated and compared to the data for fine-tuning of fitting parameters. Following the procedure described in this section, the experimental results from LSMO films are analyzed and presented in section 3.3

2.4.4   Magnetic Damping: FMR Linewidth

The FMR linewidth ΔH arises from the magnetic damping and inhomogeneities in the magnetic film [34]. Gilbert damping is shown in any magnetic system, but other relaxation channels can exist in the system and contribute to the FMR linewidth, e.g. spin pumping in FM/NM bilayer system (see section 2.5.1) and two-magnon scattering.

Two-magnon Scattering

The two-magnon scattering arises from scattering of the uniform precession of magnetization (magnons with $k = 0$ state) into magnons in a state with the same energy but a finite k-vector, $k \neq 0$, through defects presented in a thin film, see Fig. 2.6(a). Within Douglas-Mills theory of two-magnon scattering in magnetic thin films [35], the rate of two-magnon scattering depends on the structure of defects and shows anisotropic character following the in-plane symmetry of defects in the film [27, 34]. As a consequence, the FMR linewidth manifest as anisotropic as a function of the in-plane angle ϕ.

In cubic (001)-films, two-magnon scattering exhibits a *four-fold* contribution stemming from the scattering off the crystalline defects and typically presents maxima scattering rate when the magnetization is along <100> axes [34], as illustrated in Fig. 2.6(b). When defects in a stripe-like array with uniaxial symmetry are presented in the film, the two-magnon scattering with a *two-fold* symmetry could arise, as illustrated in Fig 2.6(c). The *two-fold* contribution presents the maximum (minimum) scattering rate when the magnetization is

21
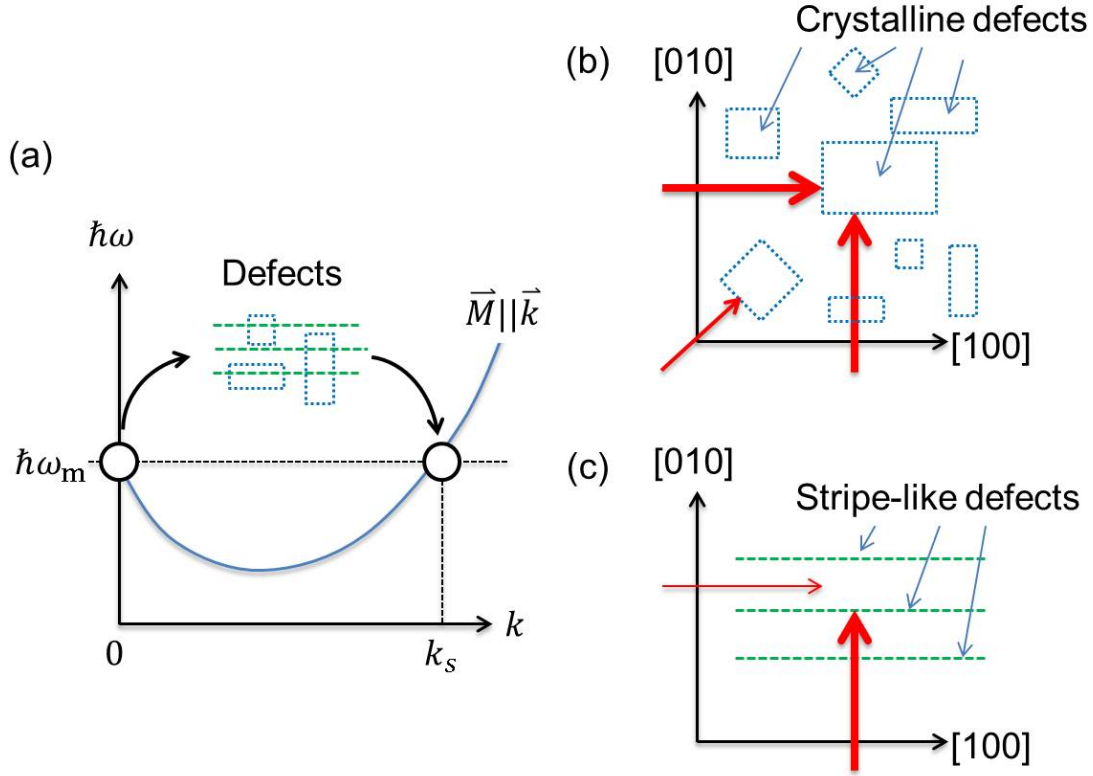
Figure 2.6: Illustrations of two-magnon scattering. (a) Uniform precession of magnetization excited by FMR can be described by magnons with $k = 0$ state. The $k = 0$ magnons can scatter by the defects presented in the film into magnons in a degenerate state with nonzero k-vector, $k_s \neq 0$. (b) A cartoon of defect matrices forming the rectangular geometry of various sizes and orientation that are randomly distributed in the film. The direction of magnetization is presented by red arrows, and the thickness represents higher scattering rate in the arrow direction. (c) A cartoon of defects forming stripe-like geometry having an uniaxial symmetry. A maximum (minimum) scattering occurs when the magnetization is perpendicular (collinear) to the stripe axis.

directed perpendicular (collinear) to the uniaxial symmetry axis [27].

2.5 Spin Pumping and Inverse Spin Hall Effect

In this section, I introduce spin pumping (SP) and inverse spin Hall effect (ISHE). In this work, the transport of spin currents through Pt/LSMO interface via spin pumping is characterized by the enhancement of FMR linewidth and confirmed by measuring the ISHE signal

as an additional support of interfacial spin transport.

2.5.1   Spin Pumping

Spin pumping [2, 3, 4] is a method of generating spin current in the NM layer of FM/NM bilayer system [36, 37, 38]. I briefly outline a basic mechanism of spin pumping based on Ref. [2, 3]. The precession of magnetization, e.g. excited by FMR in the Fig. 2.7, can dynamically polarize electrons in the NM layer near the FM/NM interface by transferring the transverse component of spin angular momentum from the FM layer. This process induces nonequilibrium spin accumulation at the FM/NM interface which then diffuses as spin current into the NM layer. When the spin current is emitted or pumped freely into the NM layer, the corresponding loss of spin angular momentum in the FM layer is necessary and act as an additional damping source of magnetization dynamics. The damping due to spin pumping α_{SP} has the same form as the Gilbert damping that the effective damping constant of the bilayer $\alpha_{\mathrm{FM/NM}}$ can be described by [2, 3]:

$$\alpha_{\mathrm{FM/NM}} = \alpha_{\mathrm{FM}} + \alpha_{\mathrm{SP}}, \tag{2.12}$$

where α_{FM} is the Gilbert damping of the isolated ferromagnet, which can be measured by analyzing the frequency dependence of FMR linewidth of a pristine FM film deposited under the identical growth condition of FM in the FM/NM bilayer. Therefore spin pump increases the linewidth of FM/NM bilayer ($\Delta H_{\mathrm{FM/NM}}$) compared to the value of the FM layer (ΔH_{FM}) without any contact to the normal metal.

The magnitude of damping due to the spin pumping α_{SP} depends on the quality of FM/NM interface and the efficiency of the spin current absorption in the normal metal. Platinum Pt is used as the normal metal in this work and assumed to have perfect absorption of spin current which is typically adopted in the literature for Pt with $t_{\mathrm{Pt}} \geq \lambda_{\mathrm{Pt}}$, where $\lambda_{\mathrm{Pt}} = 2 - 10\,\mathrm{nm}$ is
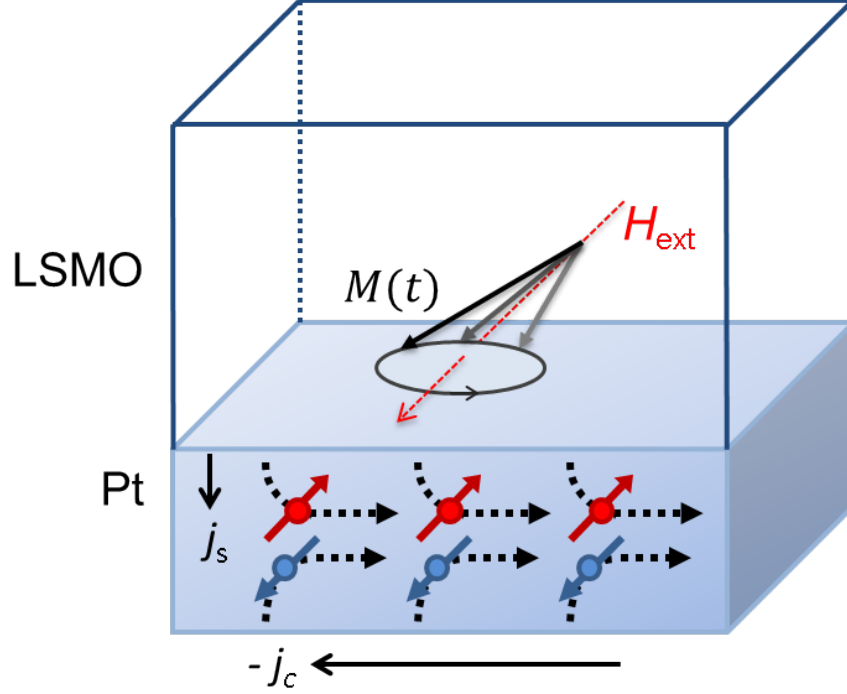
Figure 2.7: A schematic illustration of spin pumping in Pt/LSMO. $M(t)$ represents the precessing magnetization, and H_{ext} is directed in the plane of the film. Excitation of dynamical magnetization emits spin current into the adjacent Pt layer which then converted to charge current via inverse spin Hall effect in Pt. The j_{c} and j_{s} are charge and spin current density, respectively. The red and blue arrows represents spin moments μ_s.

the range of spin diffusion length in Pt [5, 37, 38, 39]. The quality of FM/NM interface for the spin transport can be characterized by the effective spin-mixing conductance $g_{\text{eff}}^{\uparrow\downarrow}$ [37, 38]:

$$\alpha_{\text{SP}} = \frac{g\mu_{\text{B}}}{4\pi M_s \, t_{\text{FM}}} g_{\text{eff}}^{\uparrow\downarrow}, \tag{2.13}$$

where μ_{B} is the Bohr magneton, g and t_{FM} are the spectroscopic splitting factor and the thickness of the ferromagnet, respectively. Therefore $g_{\text{eff}}^{\uparrow\downarrow}$ can be quantified by measuring α_{sp} from Eqn. (2.12).

DC and AC Spin Pumping

Spin current can be pictured as an equal amount of spin-up and spin-down charge currents (or electron currents) that travel in an opposite direction to each other. In this picture, charge currents are completely canceled but result in a nonzero flow of spin angular momentum [40]. Spin current is defined by the propagation direction and the orientation of the spin polarization [2, 3]. The spin current emitted by spin pumping propagates from FM/NM interface into the NM layer in the direction normal to the interface. The polarization direction of the spin current is transverse to the instantaneous orientation of the processing magnetization and therefore changes at the same frequency as the magnetization precession. However, the polarization direction can be divided into two parts having only the time-independent (DC) and dynamical time-dependent (AC) components. The DC polarization component of spin current, called DC spin pumping, is parallel to the equilibrium direction of the magnetization. So far the spin polarization is discussed in terms of spin angular momentum σ_s, but it may be beneficial to consider in term of spin moment μ_s, which is in the direction opposite to σ_s. Regarding the spin moment μ_s, the polarization of DC spin pumping is antiparallel to the equilibrium direction of the magnetization, see Fig 2.7. In this thesis, only the DC spin pumping experiments were performed, and I refer it as simply the spin pumping. A more detailed discussion of AC spin pumping can be found in Ref. [41].

2.5.2 Electrical Detection of Spin Pumping by Inverse Spin Hall Effect

The second method of measuring spin pumping is an electrical detection of the spin current by inverse spin Hall effect (ISHE), a process that converts injected spin current into charge current. ISHE is a reciprocal process of spin Hall effect (SHE), which originates from strong spin-orbit interaction [42, 43]. The normal metals that show strong spin-orbit interaction are

consist of elements with high atomic numbers also referred as heavy metals. In particular, Pt, Ta, and W have been shown to exhibit large spin Hall effect [1, 5]. By exploiting spin to charge current conversion by ISHE or vise versa by SHE in these heavy metals, spin current can be measured or generated, respectively, using the conventional charge-based electronics. In below, I describe ISHE phenomenologically by starting from spin Hall effect. As presented in Fig. 2.8(a), consider an injection of a net charge current ($\mathbf{I_c} = \mathbf{I_e^\uparrow} + \mathbf{I_e^\downarrow}$) into the heavy metal with equal amount of spin-up ($\mathbf{I_e^\uparrow}$) and spin-down charge currents ($\mathbf{I_e^\downarrow}$) that travel initially at the same direction. In the presence of strong spin-orbit interactions, each $\mathbf{I_e^\uparrow}$ and $\mathbf{I_e^\downarrow}$ experiences spin-dependent scattering processes by mechanisms such as skew-scattering, side-jump scattering, and intrinsic interactions, see Ref. [1] and the references therein. For example in Fig. 2.8(a), $\mathbf{I_e^\uparrow}$ scatter into positive y-direction while $\mathbf{I_e^\downarrow}$ scatter into negative y-direction according to the orientation of the spin polarization. The outgoing $\mathbf{I_e^\uparrow}$ and $\mathbf{I_e^\downarrow}$ propagate at an opposite direction to each other in the y-direction, hence net charge current is zero, and results spin current, net flow of spin angular momentum, in the outgoing direction. Therefore, spin Hall effect converts charge current into spin current.

The opposite process, which convert spin current into charge current, occurs for the inverse spin Hall effect. As shown in the Fig. 2.8(b), consider the spin current ($\mathbf{I_s} = \mathbf{I_e^\uparrow} - \mathbf{I_e^\downarrow}$) injected into the heavy metal in negative y direction, for example by spin pumping, and experiences the same spin-dependent scattering processes. In this case, each component of spin current $\mathbf{I_e^\uparrow}$ ($\mathbf{I_e^\downarrow}$) is initially propagating negative (positive) y-direction, which is the *opposite* direction to each other. Therefore both components scatter into the same final direction because each component has the spin polarizations opposite to each other. The result is net charge current with zero spin currents in the outgoing direction, which is x-direction in Fig. 2.8(b). The induced current generates an electric voltage in the direction perpendicular to both the propagation direction and the polarization $\hat{\sigma}_s$ of the spin current density $j_\mathbf{s}$ described by [37]

$$\vec{j_c} \parallel \vec{j_s} \times \hat{\sigma}_s, \qquad (2.14)$$
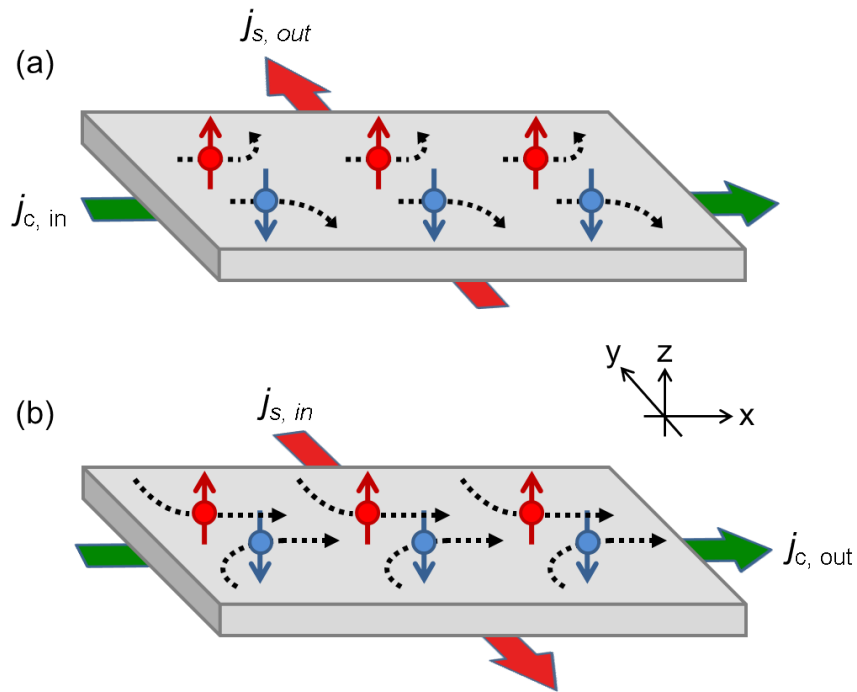
Figure 2.8: Spin Hall Effect (SHE) and inverse spin Hall effect (ISHE) in a heavy metal. (a) In the SHE process, the charge (electron) current density j_c injected in the $+\hat{x}$ is converted to the spin current density j_s outgoing in the $+\hat{y}$ with the polarization $\hat{\sigma}_s \parallel +\hat{z}$. (b) In the ISHE process, the spin current density j_s with the polarization $\hat{\sigma}_s \parallel +\hat{z}$ is injected into the $-\hat{y}$ and converted into the charge current density j_c outgoing in the $+\hat{x}$. Arrows represent spin angular momentum σ_s which is in the direction opposite to the spin moment μ_s.

where $\vec{j}_c$ and $\vec{j}_s$ describe the charge current density and spin current density, respectively. The polarization of spin current emitted into the heavy metal by spin pumping has the DC component parallel to the equilibrium direction of the magnetization. In the saturated regime, $H > H_{\mathrm{sat}}$, the equilibrium direction of the magnetization, hence the DC polarization of the spin current is along the external magnetic field direction. Therefore the ISHE generates the DC voltage, which I call ISHE signal, in the direction perpendicular to the direction of the external magnetic field in the plane of the film. The lineshape of ISHE signal V_{sp} is purely Lorentzian [44] and the dependence of in-plane magnetic field direction leads to the reversal of the amplitude sign under the change $H_{\mathrm{ext}} \rightarrow -H_{\mathrm{ext}}$.

$$V_{\mathrm{sp}}(H_{\mathrm{ext}}) = -V_{\mathrm{sp}}(-H_{\mathrm{ext}}) \tag{2.15}$$

2.5.3 Experimental Setup for ISHE Measurements

Figure 2.9 shows a setup for *in situ* measurements of ISHE signal and FMR. A CPW unit similar to the CPW used in the FMR measurement is modified by adding trenches in the ground planes. The trenches are created by machining at vertical mills without any fluids. The end mills with small diameters determined the trench width and pre-cleaned with acetone and isopropyl alcohol (IPA) to avoid any oil contamination on the CPW. Although machining CPW is easy, some care is given for securing the CPW as it is thin and could be bendable. The area inside trenches defines a conductor pad, and the pad is physically and electrically isolated from the ground plane of the CPW. Next, DC wires are soldered onto the pads for an easy and secure connection from these pads to the lock-in amplifier or a voltmeter. The Pt/LSMO bilayer film is placed face downward onto the Teflon tape which isolates the film from the signal line of CPW. The film is secured by applying silver epoxy onto the edges of film that extends to each isolated pads and letting it completely dry, see Fig. 2.9(b). The dried silver epoxy also provides a robust electrical connection from the

edge of bilayer film to the pad. The silver epoxy is stored in a cold fridge and pre-warm up, approximately 5 min outside, helps to apply it in uniform density.

As FMR absorption is excited predominantly in the area of the film just above the signal line, the ISHE signal is generated in Pt layer between the edges of the signal line. Ideally electrical contacts from the pads to the bilayer should be made as close as to the edges of the signal line otherwise loss of ISHE signal occur by shunting through additional conducting areas beyond where the ISHE signal is generated. A practical solution is to create the trenches as close as possible to vias without damaging them, see Fig. 2.9(c). Otherwise, the transmission quality of CPW can be modified.

Microwave Eddy Currents Induced by CPW

In this work, the ISHE signal of Pt(9 nm) capped LSMO(20 nm) bilayer film is measured using the modified CPW setup described in the previous section. When a conductive film (typically 20-30 $\mu\Omega \cdot$ cm for Pt(5 nm) film [45, 39] or Py(10 nm) film [46]) is brought close to the CPW, the distributions of electric and magnetic microwave fields of CPW can be strongly modified. This effect is described regarding the microwave field shielding by eddy currents induced in the conducting film, which can occur much below the microwave skin depth of ferromagnets [46, 47].

In Ref. [46], a setup consist of conventional CPW with a conductive film on top separated by an air gap of 30 μm is simulated by COMSOL Multiphysics. The simulation showed that the shielding of the electric and magnetic microwave field depends on the square resistance of the film, transverse dimensions of CPW and microwave frequency. For example, within 0.1-20 GHz range, the electric microwave field would be completely shielded by Pt(5 nm) film while the shielding of the magnetic microwave is incomplete. This result implies that the eddy currents enough to shield the electric microwave field is expected to occur in the Pt(9 nm) layer of the Pt/LSMO bilayer and the flow direction is collinear to the magnetic
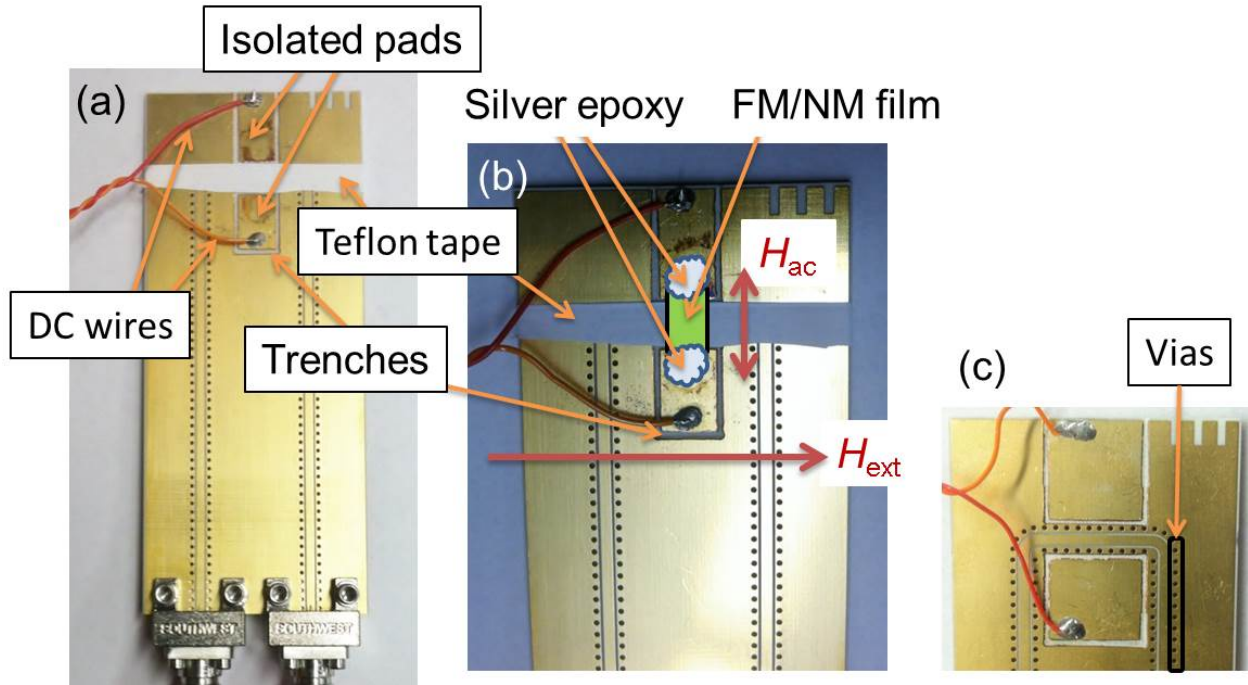
Figure 2.9: A CPW for *in situ* FMR and ISHE measurements (a) The CPW board with machined out trenches define electrically isolated pads. The soldered DC wires on each pad are connected to a lock-in amplifier or a voltmeter. Teflon tapes are cut into small width to cover up only the signal line and vias of the CPW. (b) An FM/NM film, presented by a green cartoon rectangle, is placed faced downward onto the CPW and the signal line is isolated by the Teflon tape. The film is attached to the pads by silver epoxy, represented as light blue cartoon picture, which provides electrical connections. The external magnetic field is directed collinear to the signal line and transverse to the driving microwave magnetic field H_{RF} to perform spin pumping, and the maximum ISHE signal is induced in the direction perpendicular to the external magnetic field. (c) A close-up picture is showing a different CPW modified for the ISHE measurement. The picture shows machined out trenches as close as possible to Vias. The large-sized isolated pads in this CPW are made to accommodate films having large lateral dimensions.

microwave field H_{RF}. Although not enough to result in a complete shielding, the magnetic microwave field is expected to drive eddy current in the bilayer that flows in the direction collinear to the signal line of CPW (perpendicular to the H_{RF}) [47]. When considering small misalignments in the experimental setup, eddy currents in the Pt/LSMO bilayer driven by the microwave EM field of CPW in all lateral direction is expected in this work.

DC Voltage Induced by Rectification Effects

In FM/NM bilayer system, additional DC voltage can be induced from rectification of microwave currents by resistance oscillations. The microwave eddy current can be induced in the conductive film by the EM field of the CPW as described in the previous section. When the magnetization dynamics is excited, the resistance oscillations arise from anisotropic magnetoresistance (AMR) or anomalous Hall effect (AHE) of the ferromagnet [33, 44]. The rectified voltage can have contributions from both symmetric and antisymmetric Lorentzian and need to be distinguished from ISHE signal induced by spin pumping [44].

All experimental configurations in combinations of the directions of H_{RF}, microwave current and DC voltage that the rectification voltage can occur are summarized in Ref. [44], and the lineshapes of the rectification voltage and angular dependences are shown in ibid., Table 3 and Table 4, respectively. In this work, the ISHE signal is measured in the direction perpendicular to bias external magnetic field H_{ext}. This measurement geometry is in high symmetry where the rectification voltage vanishes except for two configurations. These configurations are 1) the microwave current I_{RF} flowing in the direction of H_{ext} with the out-of-plane H_{RF} or 2) with the in-plane H_{RF} in the direction perpendicular to I_{RF}, see Table 4 in the Ref. [44]. The direction of magnetic microwave field H_{RF} lies in the plane and transverse to the signal line in general and has a nonzero component in the out-of-plane direction near the edge of the signal line, see section 2.4.1. In this work, the maximum RF power, $+25\,\mathrm{dBm}$, from the microwave generator (Hittite, Model HMC-T2220) is applied to get ISHE signal with

SNR ratio. At this high RF power, the contribution of out-of-plane component of H_{RF} to the FMR excitation can become more significant than in the typical CPW-FMR measurements at low RF power, 5-$10\,\mathrm{dBm}$. Each AMR-based and AHE-based rectification voltage in these two configuration has different line shapes and the symmetry under $180°$ rotation $H_{\mathrm{ext}} \to -H_{\mathrm{ext}}$. These features will be used to distinguish the ISHE signal of spin pumping from the rectification voltage.

Chapter 3

Results and Discussions

3.1 Growth of LSMO Thin Films

The LSMO films and the X-ray diffraction (XRD) characterizations in this work are provided by the H. Y. Hwang group at Stanford University. LSMO thin films were grown on TiO_2-terminated $SrTiO_3(001)$ (STO) substrates by pulsed laser deposition (PLD) as described in Ref. [17]. Enhanced metallicity in the thin limit (≥ 7 unit cells) with high Curie temperature $T_C \approx 360\,K$ are exhibited in the films grown under these conditions [17]. During growth, the thickness of LSMO film was monitored by *in situ* reflection high-energy electron diffraction (RHEED) and all LSMO films with various thicknesses appear in this thesis was grown under the same conditions. The XRD structural characterization of the LSMO(25 nm) thin film is shown in Fig. 3.1(a). The θ-2θ scan around the STO (002) peak shows finite thickness fringe patterns of a uniform, highly crystalline, epitaxial LSMO film. Figure. 3.1(b) shows the reciprocal space map of the (103) peak which confirms the fully strained LSMO thin films to the substrate and epitaxially grown along the (001) orientation. Pt layer was deposited *ex situ* using an e-beam evaporator for Pt/LSMO bilayer films.
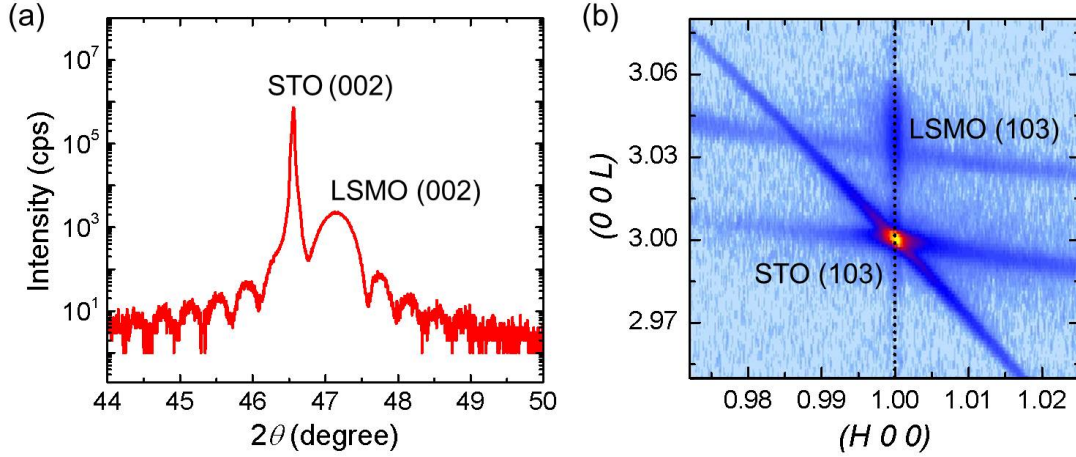
Figure 3.1: X-ray diffraction of epitaxial LSMO(25 nm) on STO (001) substrate. (a) θ-2θ scan near the (002) peak. (b) Reciprocal space map near the (103) peak.

3.2 Ferromagnetic Resonance of LSMO Thin Films

I employ coplanar waveguide (CPW) based broadband ferromagnetic resonance (FMR) with magnetic field modulation to measure magnetic properties of LSMO films and Pt/LSMO bilayers. All measurements are performed at room temperature. A typical FMR spectrum shown in Fig. 3.2 is well fit by a single absorption profile described by the field derivative of a sum of symmetric and antisymmetric Lorentzians [30]. Previously, LSMO thin films typically shown to exhibit a strong satellite absorption peak [48]. This mode has a negligible amplitude in the samples, and I will focus discussions on the dominant FMR mode.

3.3 LSMO(30 nm) on STO(001)

3.3.1 Magnetic Anisotropy

First, I study the magnetic anisotropy of uncapped LSMO(30 nm) thin films. Figure 3.3(a) shows the resonance field as a function of in-plane magnetic field angle ϕ_H with respect
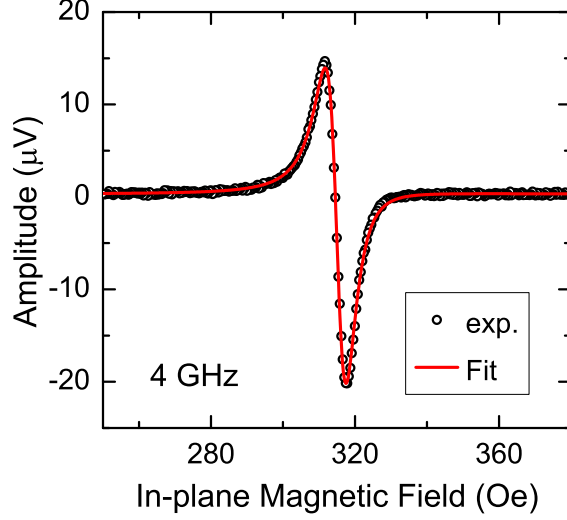
Figure 3.2: A typical field-modulated FMR spectrum of LSMO(30 nm) measured by a sweeping magnetic field at a constant 4 GHz. FMR spectrum is well fitted to a single FMR absorption profile described by Eqn. (2.10).

to the [100] axis. The data shows a dominant uniaxial magnetic anisotropy (UMA) with its easy axis parallel to the [010] crystallographic axis at $\phi_H = 90°$. Frequency-dependent FMR measurements shown in Fig. 3.3(b) confirm the uniaxial character as the data taken at $\phi_H = 0°$ presents typical hard axis FMR dispersion with a curvature near saturation field $H_{\text{sat}} \simeq 46$ Oe. Based on these observations, the total free energy density [24] of magnetization is model by:

$$F_{\text{total}} = -\vec{M} \cdot \vec{H} + \frac{1}{2} M_{\text{s}} H_1 \cos^2 \theta$$
$$- \frac{1}{16} M_{\text{s}} H_{\text{mc}} (7 + \cos 4\phi) \sin^4 \theta$$
$$- \frac{1}{2} M_{\text{s}} H_{\text{uni}} \cos^2(\phi - \phi_{\text{uni}}) \sin^2 \theta, \tag{3.1}$$

where θ and ϕ are the polar and azimuthal angles of the magnetization $\vec{M}$ measured from [001] and [100], respectively, and $\vec{H}$ is the external magnetic field. The first term in Eq. (3.1) is the Zeeman energy. The second term is the effective out-of-plane magnetic anisotropy with $H_1 = 4\pi M_{\text{s}} - 2K_\perp/M_{\text{s}} - H_{\text{mc}}$, where $K_\perp$ is the perpendicular magnetic anisotropy (PMA).
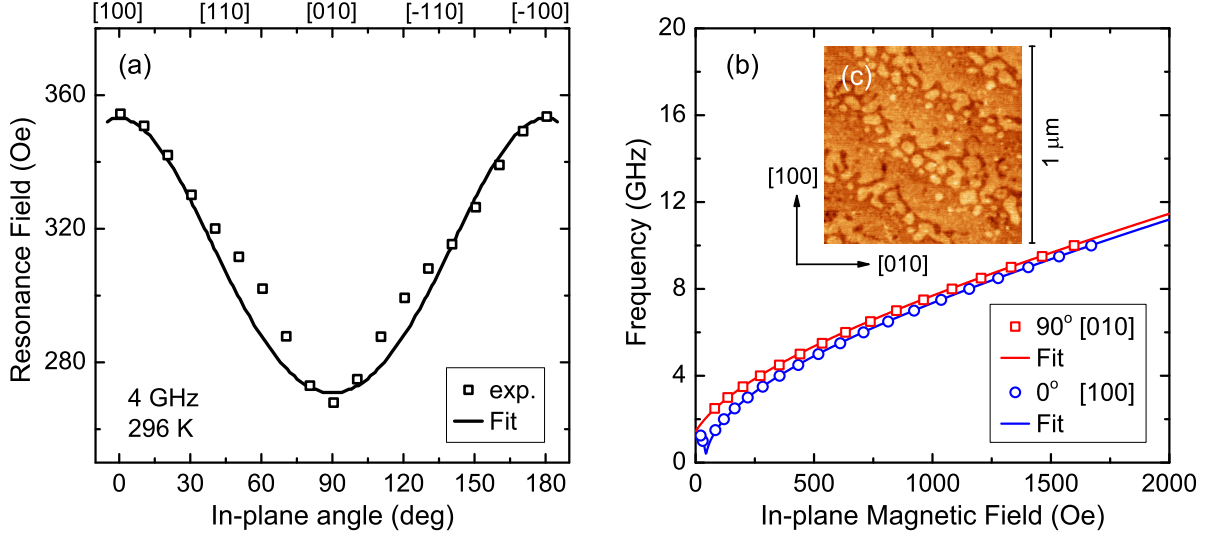
Figure 3.3: LSMO(30 nm) (a) FMR resonance field vs in-plane angle ϕ_H measured at 4 GHz. (b) Frequency vs resonance field for easy axis (squares) and hard axis (circles). (c) AFM topography of the LSMO surface. The AFM image shows terraces with step-edge orientation of 125° with respect to [100]. Data are taken at room temperature and all error bars are smaller than the symbol size.

The third term describes the four-fold magnetocrystalline anisotropy (MCA) with effective field $H_{\mathrm{mc}} = 2K_{\mathrm{mc}}/M_{\mathrm{s}}$. The last term is the in-plane UMA with anisotropy field H_{uni} and its easy axis at ϕ_{uni}.

The Smit and Beljers formalism [24, 28] is used to fit the FMR data:

$$\left(\frac{2\pi f}{\gamma}\right)^2 = \frac{1}{M_{\mathrm{s}}^2 \sin^2\theta}\left[\frac{\partial^2 F}{\partial\theta^2}\frac{\partial^2 F}{\partial\phi^2} - \left(\frac{\partial^2 F}{\partial\theta\partial\phi}\right)^2\right], \tag{3.2}$$

where f is the resonance frequency, $\gamma = g\mu_{\mathrm{B}}/\hbar$ is the gyromagnetic ratio with spectroscopic splitting factor g and μ_{B} is the Bohr magneton. Eqn. (3.2) is evaluated at the equilibrium angles θ_{eq} and ϕ_{eq} obtained from minimization of the free energy density in Eqn. (3.1).

I employ Eqn. (3.2) to simultaneously fit the frequency- and angle-dependent FMR data in Fig. 3.3(a,b) with g, H_1, H_{mc}, H_{uni} and ϕ_{uni} as fitting parameters, see section 2.4.3 for details. The small differences between the experimental data and the fit in Fig. 3.3(a) cannot be reduced even by introducing the second-order MCA term (not shown here). The best fit

returns $g = 1.975$ and $H_1 = 6380\,\mathrm{Oe}$, which are similar to the values reported in Ref. [49] and Refs. [50, 51], respectively. At this room temperature measurement, MCA field is found to be negligibly small ($|H_{\mathrm{mc}}| < 1\,\mathrm{Oe}$) despite the epitaxial nature of our LSMO films. The in-plane magnetic anisotropy is dominated by the UMA term with $H_{\mathrm{uni}} = 42\,\mathrm{Oe}$ and $\phi_{\mathrm{uni}} = 90°$ given by the best fit. With room-temperature value of $M_{\mathrm{s}} \approx 265\,\mathrm{emu/cm^3}$ [17] and the negligibly small MCA field H_{mc}, our epitaxial LSMO films on STO(001) exhibit negative PMA ($K \approx -4.0 \times 10^5\,\mathrm{erg/cm^3}$) comparable to previous reports [50, 51]. The negative PMA results in-plane preference of magnetization and positively adds to the shape anisotropy, see section 2.2. The UMA was previously observed in LSMO films grown on STO(001) and its easy axis was found to be parallel to the atomic terrace edges of the miscut substrate [52, 53]. Figure 3.3(c) shows atomic force microscope (AFM) topography of the same film investigated by FMR. The AFM image shows step-and-terrace features with $0.39\,\mathrm{nm}$ step height consistent with single LSMO unit cell [17], and approximately $250\,\mathrm{nm}$ terrace width stemming from a slight miscut of the STO substrate. The step edges of the terraces are oriented at $125°$ with respect to [100] and this orientation is not correlated with either the symmetry axes of the crystal or the measured uniaxial magnetic anisotropy. Therefore the origin of uniaxial magnetic anisotropy is not related to the substrate miscut and its origin remains unclear.

3.3.2 Magnetic Damping

I analyze the FMR linewidth data to quantify magnetic damping of our LSMO films. The linewidth is found to be strongly angular dependent in the film plane with a four-fold and a two-fold components as shown in Fig. 3.4(a). Such anisotropic linewidth has been experimentally observed in other epitaxial film systems and explained in terms of two-magnon scattering that follows the in-plane symmetry of defects in the film [27, 34, 35, 54]. In particular, the four-fold contribution in cubic (001)-films arises from crystalline defects and
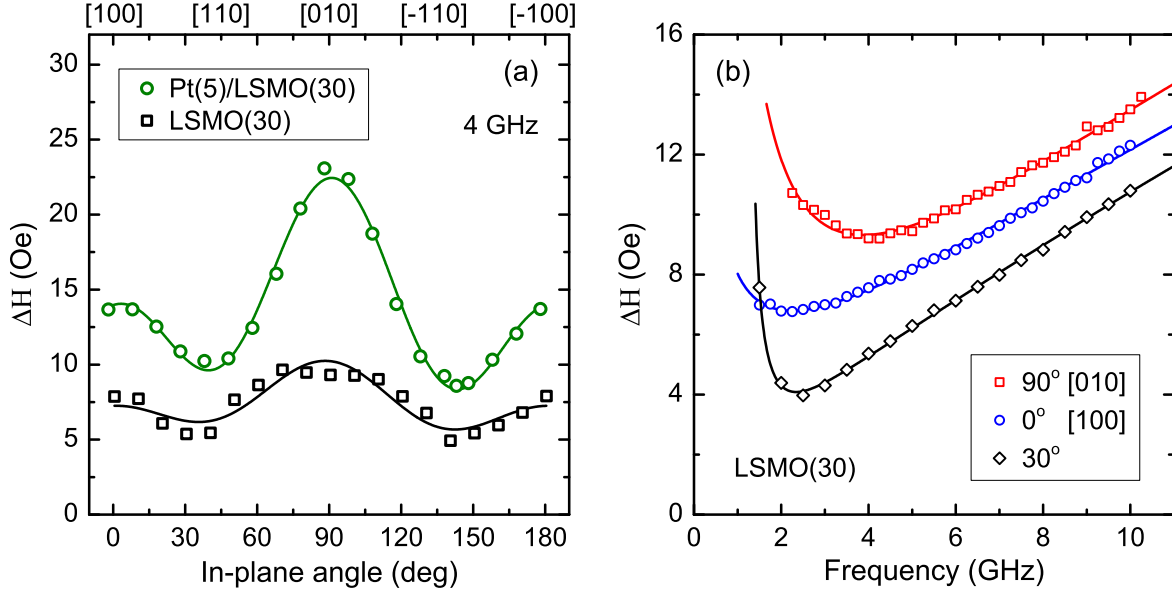
Figure 3.4: (a) FMR linewidth (ΔH) as a function of in-plane magnetic field angle ϕ_H for LSMO (squares) and Pt/LSMO (circles) films at 4 GHz. (b) Frequency-dependent FMR linewidth for the LSMO film at three values of ϕ_H. The lines show the best fit.

typically presents maxima along <100> axes [34]. The two-fold contribution arises from defects with uniaxial, stripe-like symmetry and presents maxima at directions perpendicular to the uniaxial symmetry axis [27]. Based on Refs. [27, 34], the FMR linewidth ΔH (half width at half maximum) can be formulated by following ansatz:

$$\Delta H = \Delta H_{\mathrm{LF}} + \Delta H_{\mathrm{inh}} + \frac{2\pi f \alpha}{\gamma \Psi} + \frac{\sum_j \Gamma_{\mathrm{2m}}^{ij}}{\gamma \Psi} \tag{3.3}$$

The first term describes the low-frequency contribution that arises from inhomogeneous microwave field of the CPW. It has the form $\Delta H_{\mathrm{LF}} \propto f^{-\rho}$ [55, 56]. The second term represents the line broadening due to inhomogeneity of the sample and has two components: a constant term and a mosaicity term of the form $\propto \partial H_{\mathrm{r}}/\partial \phi_H$ [34, 57]. The third term describes Gilbert-type damping which is proportional to the Gilbert constant α. It includes a correction factor $\Psi = \cos(\phi - \phi_H)$ accounting for the field dragging effect [57]. The last term reflects the two-magnon scattering with $\Gamma_{\mathrm{2m}}^{ij} = \Gamma_i^j \xi_i^j(\phi)\zeta(f)$, where i and j are indices labeling the symmetry of the two-magnon scattering channel and the axis of the maximum

scattering rate for this channel, respectively. The corresponding scattering rates are Γ_i^j. As described in Refs. [27, 34, 35, 54], $\xi_2^j(\phi) = \cos^4(\phi - \phi_{2,j}^{\max})$ for the two-fold symmetry channel and $\xi_4^j(\phi) = \cos^2(2(\phi - \phi_{4,j}^{\max}))$ for the four-fold symmetry channel, where $\phi_{i,j}^{\max}$ is the angle of the maximum scattering rate. The frequency dependence $\zeta(f)$ of the two-magnon scattering is described in Ref. [35]. Due to the distinctive angular- and frequency-dependence of each term in Eqn. (3.3), I can unambiguously fit the data in Fig. 3.4 and extract all damping parameters.

From the fit shown in Fig. 3.4(a), the rates of two-magnon scattering with four-fold and two-fold contributions are $\Gamma_4^{\langle 100 \rangle} = 2.4(3) \times 10^8 \, \text{Hz}$, $\Gamma_4^{\langle 110 \rangle} = 0.9(3) \times 10^8 \, \text{Hz}$, and $\Gamma_2^{[010]} = 2.5(4) \times 10^8 \, \text{Hz}$, respectively. The four-fold two-magnon scattering shows maxima along $\langle 100 \rangle$, as expected for the (001) film [34]. The two-fold term $\Gamma_2^{[010]}$ presents maximum at [010]. This direction does not correspond to either the hard axis of the UMA in contrast to the expected behavior [27] or to the terrace orientation observed in AFM topography. In fact, the stripe-like terraces of the LSMO film generate a weak additional two-fold two-magnon scattering channel with $\Gamma_2^{\perp \text{step}} = 0.4(4) \times 10^8 \, \text{Hz}$ at $\phi_{2,\perp \text{step}}^{\max} = 35°$ which is the perpendicular to the step-edge orientation ($\phi = 125°$) as expected [27].

The best fit gives the Gilbert constant $\alpha_{\text{LSMO}} = 1.9(1) \times 10^{-3}$. This value is low among reported values of LSMO films on STO(001) [48, 58]. Also, this value is comparable to the lowest values reported for metallic ferromagnetic films: $\alpha = 2.3 \times 10^{-3}$ in epitaxial $Fe_{1-x}Si_x$ [59], 2.1×10^{-3} in epitaxial Fe-V alloy [60], and 1.0×10^{-3} in Co_2FeAl [61]. The inhomogeneous line broadening is found to be small for our LSMO films $\Delta H_{\text{inh}} = 1.3 \, \text{Oe}$, with a negligible mosaicity contribution $\leq 0.7 \, \text{Oe}$.

3.4   Pt(5 nm)/LSMO(30 nm) on STO(001)

3.4.1   Magnetic Anisotropy and Damping

Next, I study the effect of adding a Pt capping layer to LSMO films. The best fit to the resonance field data of Pt(5 nm)/LSMO(30 nm) film returns $g = 1.975$, $H_1 = 6410$ Oe, and $|H_{\mathrm{mc}}| < 3$ Oe. These values are very similar to those of the bare LSMO film. The UMA field $H_{\mathrm{uni}} = 36$ Oe decreases by 14% while retaining its easy axis along [010]. The FMR linewidth analysis shows that the two-magnon scattering rates are significantly increased compared to the bare LSMO film without change of their symmetry: $\Gamma_2^{[010]} = 7.3(2) \times 10^8$ Hz, and $\Gamma_4^{\langle 100 \rangle} = 5.7(1) \times 10^8$ Hz. The two-fold two-magnon term due to terrace step-edges is $\Gamma_2^{\perp \mathrm{step}} = 1.1(2) \times 10^8$ Hz, and the four-fold two-magnon due to 45°-rotated crystalline defects is $\Gamma_4^{\langle 110 \rangle} = 0.4(1) \times 10^8$ Hz. These findings suggest a modification of the LSMO surface due to Pt deposition and impact the two-fold and four-fold two-magnon scattering. The FMR linewidth of the Pt/LSMO film versus frequency exhibits multiple peaks, as shown in Fig. 3.5(a), that are are absent for the bare LSMO film in Fig. 3.4(b). Near the frequency values marked as A and B in Fig. 3.5(a), the FMR absorption profile is significantly distorted as shown in Fig. 3.5(b,c). Previously, a similar effect was reported for permalloy (Py) films with a periodic array of stripe-like defects. For Py, the peaks in the linewidth were found to disappear when the film was magnetized parallel to the stripe-like defects [59, 62]. The absence of the peaks in our linewidth data for magnetization along the [100] axis in Fig. 3.5(a) suggests that the Pt/LSMO bilayer films develop stripe-like magnetic defects oriented along this axis.
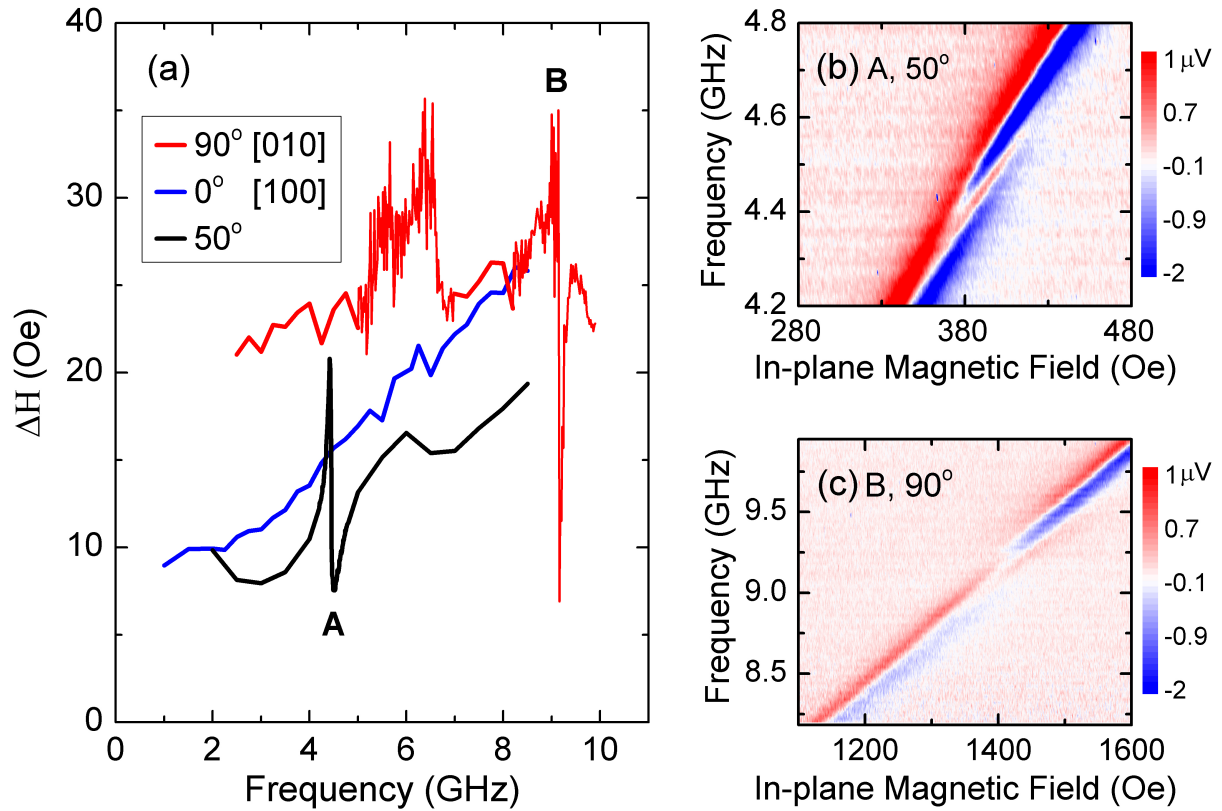
Figure 3.5: Pt(5 nm)/LSMO(30 nm) bilayer (a) Frequency-dependent FMR linewidth for three values of ϕ_H. Multiple peaks seen in the FMR linewidth as a function of frequency are due to distortions of the FMR absorption profile evident in (b) and (c): color plots of the measured FMR signal versus frequency and magnetic field near frequencies marked A and B in (a).

3.4.2 Spin Pumping

Another important effect of the Pt layer is the increase of the Gilbert damping constant due to spin pumping, a process in which spin angular momentum is dynamically injected from the LSMO into the adjacent Pt layer [2, 4]. I fit the frequency- and angle-dependent linewidth data for the Pt/LSMO bilayer to quantify the Gilbert constant. In this fitting procedure, I omit the linewidth data in the frequency intervals that exhibit peaks (such as frequencies marked as A and B in Fig. 3.5). The estimated the Gilbert constant is $\alpha_{\text{Pt/LSMO}} \approx 2.9(5) \times 10^{-3}$, which is $\sim 50\%$ higher than the value of the bare LSMO film but still lower than a typical Py film system.

The effective interfacial spin mixing conductance $g_{\text{eff}}^{\uparrow\downarrow}$ can be determined [2, 3, 37, 38] from:

$$g_{\text{eff}}^{\uparrow\downarrow} = \frac{4\pi M_{\text{s}}\, t_{\text{LSMO}}}{g\mu_{\text{B}}}(\alpha_{\text{Pt/LSMO}} - \alpha_{\text{LSMO}}) \tag{3.4}$$

For the 30 nm thick film, $t_{\text{LSMO}} = 30 \times 10^{-7}$ cm with $M_{\text{s}} \approx 265\,\text{emu/cm}^3$, I estimate $g_{\text{eff}}^{\uparrow\downarrow} \approx 0.55 \times 10^{15}\,\text{cm}^{-2}$. This number is comparable to the mixing conductance of Pt/Py films $(2.1 \times 10^{15}\,\text{cm}^{-2})$ [37, 38] that reflects significant spin transport across the Pt/LSMO interface despite of the *ex situ* deposition of Pt.

For direct confirmation of the spin pumping process, ISHE signal is measured in the Pt/LSMO bilayer at the direction perpendicular to the external magnetic field, see section 2.5.3 for more details. The ISHE signal is DC voltage that arises from the spin pumping via the inverse spin Hall effect in the Pt layer, and it has lineshape described by symmetric Lorentzian [44]. A simultaneous measurement of FMR and ISHE signal is shown in Fig. 3.6. For the Pt/LSMO bilayer, a weak satellite mode is visible next to a dominant FMR absorption profile. The two modes are well identified in the fitting, and I will focus discussions on the dominant FMR mode. These measurements are performed under field modulation scheme using two lock-in amplifiers.

In the field modulation scheme, the symmetric (antisymmetric) Lorentzian appears as the
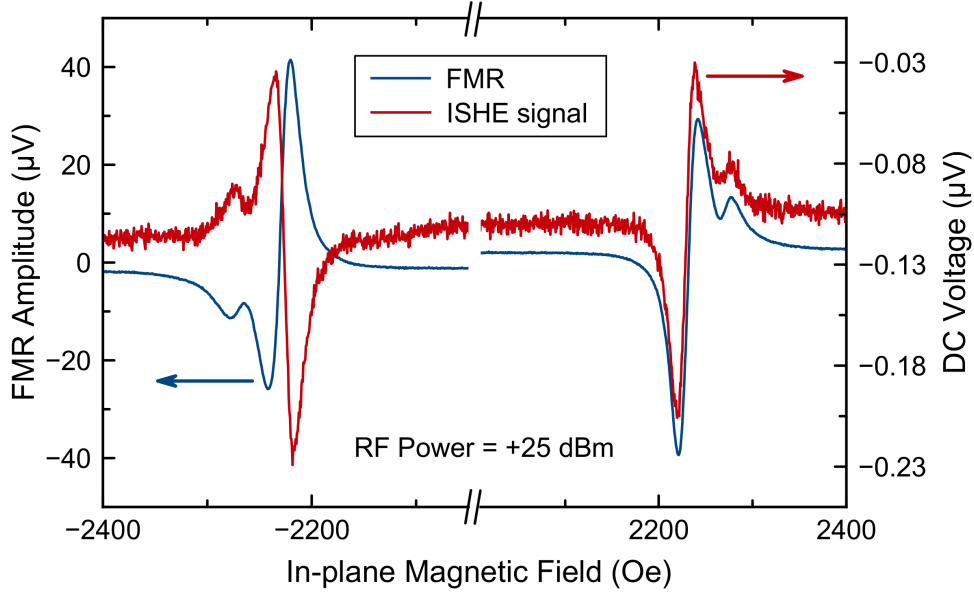
Figure 3.6: Field-modulated ISHE signal (red) and the corresponding FMR signal (blue) of Pt(9 nm)/LSMO(20 nm) film measured at $12\,\mathrm{GHz}$ and $+25\,\mathrm{dBm}$ RF power applied to the CPW.

antisymmetric (symmetric) profile with respect to the resonance field H_r, respectively. The predominant symmetry of ISHE signal in Fig. 3.6 (red line) is an antisymmetric profile and therefore described by the field derivative of the symmetric Lorentzian. Also, the ISHE signal (red line) tracks closely to that of the absorptive FMR signal (blue line) and changes sign upon reversal of the magnetic field polarity $H_{\mathrm{ext}} \to -H_{\mathrm{ext}}$, indicating the spin pumping as the origin [37, 44].

The ISHE signal in Fig. 3.6 has a small antisymmetric Lorentzian contribution which can arise from the rectification effects. A fit to the ISHE signal, not shown here, returns no change in the amplitude sign of the antisymmetric Lorentzian contribution under $H_{\mathrm{ext}} \to -H_{\mathrm{ext}}$ and attribute to AHE-based rectification voltage based on Ref. [44]. Furthermore, the associated symmetric Lorentzian component of AMR-based rectification voltage does not result in the sign reversal, see column 4 in Table 4 of Ref. [44]. Therefore the rectification voltage in the bilayer cannot account the sign reversal of ISHE signal under $H_{\mathrm{ext}} \to -H_{\mathrm{ext}}$ and confirms the spin pumping origin of the ISHE signal.

Chapter 4

Conclusion and Perspectives

In conclusion, I measured room-temperature magnetic anisotropy and damping in epitaxial LSMO films and Pt/LSMO bilayers grown on STO(001) substrates. I find significant uniaxial magnetic anisotropy, weak magnetocrystalline anisotropy, and strong negative perpendicular magnetic anisotropy that remain unaffected by the Pt cap. The easy axis of the dominant uniaxial magnetic anisotropy is parallel to the [010] crystallographic axis. Both LSMO and Pt/LSMO systems exhibit significant anisotropic magnetic damping with four-fold and two-fold symmetry components which are attributed to arise from two-magnon scattering. The four-fold component is aligned with the in-plane principal crystallographic axes and can be attributed to two-magnon scattering on crystalline defects. The symmetry axis of the two-fold two-magnon is parallel to the [010] crystallographic axis, and its origin remains unexplained. I find that a Pt capping layer enhances the anisotropic two-magnon scattering and increases Gilbert damping in Pt/LSMO system. I attribute the Gilbert damping enhancement to spin current flow across the Pt/LSMO interface induced by spin pumping. The relatively high spin mixing conductance and the very low Gilbert damping (comparable with the best-reported values of other metallic ferromagnets) are found, which make Pt/LSMO an attractive system for spintronic applications such as spin Hall memories [6] and oscillators

[10, 12, 13, 63, 64]. Lastly, these results indicate that LSMO is a promising building block for all-oxide perovskite-based spintronics devices.

Bibliography

[1] J. Sinova, S. O. Valenzuela, J. Wunderlich, C. H. Back, and T. Jungwirth. Spin Hall effects. *Rev. Mod. Phys.*, 87:1213–1260, 2015.

[2] Y. Tserkovnyak, A. Brataas, and G. E. W. Bauer. Enhanced Gilbert damping in thin ferromagnetic films. *Phys. Rev. Lett.*, 88:117601, 2002.

[3] Y. Tserkovnyak, A. Brataas, and G. E. W. Bauer. Spin pumping and magnetization dynamics in metallic multilayers. *Phys. Rev. B*, 66:224403, 2002.

[4] R. Urban, G. Woltersdorf, and B. Heinrich. Gilbert damping in single and multilayer ultrathin films: role of interfaces in nonlocal spin dynamics. *Phys. Rev. Lett.*, 87:217204, 2001.

[5] A. Hoffmann. Spin Hall effects in metals. *IEEE Trans. Magn.*, 49:5172–5193, 2013.

[6] L. Liu, C.-F. Pai, Y. Li, H. W. Tseng, D. C. Ralph, and R. A. Buhrman. Spin-torque switching with the giant spin Hall effect of tantalum. *Science*, 336:555–558, 2012.

[7] L. Liu, T. Moriyama, D. C. Ralph, and R. A. Buhrman. Spin-torque ferromagnetic resonance induced by the spin Hall effect. *Phys. Rev. Lett.*, 106:036601, 2011.

[8] J.-C. Rojas-Sánchez, N. Reyren, P. Laczkowski, W. Savero, J.-P. Attané, C. Deranlot, M. Jamet, J.-M. George, L. Vila, and H. Jaffrès. Spin pumping and inverse spin Hall effect in platinum: the essential role of spin-memory loss at metallic interfaces. *Phys. Rev. Lett.*, 112:106602, 2014.

[9] B. Heinrich, C. Burrowes, E. Montoya, B. Kardasz, E. Girt, Y.-Y. Song, Y. Sun, and M. Wu. Spin pumping at the magnetic insulator (YIG)/normal metal (Au) interfaces. *Phys. Rev. Lett.*, 107:066604, 2011.

[10] M. Collet, X. de Milly, O. d'Allivy Kelly, V. V. Naletov, R. Bernard, P. Bortolotti, J. Ben Youssef, V. E. Demidov, S. O. Demokritov, J. L. Prieto, M. Muñoz, V. Cros, A. Anane, G. de Loubens, and O. Klein. Generation of coherent spin-wave modes in yttrium iron garnet microdiscs by spinorbit torque. *Nat. Commun.*, 7:10377, 2016.

[11] H. L. Wang, C. H. Du, Y. Pu, R. Adur, P. C. Hammel, and F. Y. Yang. Scaling of spin Hall angle in 3d, 4d, and 5d Metals from $Y_3Fe_5O_{12}$/metal spin pumping. *Phys. Rev. Lett.*, 112:197201, 2014.

[12] V. E. Demidov, S. Urazhdin, H. Ulrichs, V. Tiberkevich, A. Slavin, D. Baither, G. Schmitz, and S. O. Demokritov. Magnetic nano-oscillator driven by pure spin current. *Nat. Mater.*, 11:1028–1031, 2012.

[13] Z. Duan, A. Smith, L. Yang, B. Youngblood, J. Lindner, V. E. Demidov, S. O. Demokritov, and I. N. Krivorotov. Nanowire spin torque oscillator driven by spin orbit torques. *Nat. Commun.*, 5:5616, 2014.

[14] K. Gilmore, Y. U. Idzerda, and M. D. Stiles. Spin-orbit precession damping in transition metal ferromagnets. *J. Appl. Phys.*, 103:07D303, 2008.

[15] S. Majumdar and S. van Dijken. Pulsed laser deposition of $La_{1-x}Sr_xMnO_3$: thin-film properties and spintronic applications. *J. Phys. D: Appl. Phys.*, 47:034010, 2014.

[16] M. Bowen, M. Bibes, A. Barthelemy, J. P. Contour, A. Anane, A. Lemaitre, and A Fert. Nearly total spin polarization in $La_{2/3}Sr_{1/3}MnO_3$ from tunneling experiments. *Appl. Phys. Lett.*, 82:233–235, 2003.

[17] B. Kim, D. Kwon, J. H. Song, Y. Hikita, B. G. Kim, and H. Y. Hwang. Finite size effect and phase diagram of ultra-thin $La_{0.7}Sr_{0.3}MnO_3$. *Solid State Commun.*, 150:598–601, 2010.

[18] C. Liu, C. K. A. Mewes, M. Chshiev, T. Mewes, and W. H. Butler. Origin of low Gilbert damping in half metals. *Appl. Phys. Lett.*, 95:022509, 2009.

[19] J. H. Song, T. Susaki, and H. Y. Hwang. Enhanced thermodynamic stability of epitaxial oxide thin films. *Adv. Mater.*, 20:2528–2532, 2008.

[20] L. F. Kourkoutis, J. H. Song, H. Y. Hwang, and D. A. Muller. Microscopic origins for stabilizing room-temperature ferromagnetism in ultrathin manganite layers. *Proc. Natl. Acad. Sci.*, 107:11682–11685, 2010.

[21] Y. Hikita, M. Nishikawa, T. Yajima, and H. Y. Hwang. Termination control of the interface dipole in $La_{0.7}Sr_{0.3}MnO_3$/Nb:$SrTiO_3$ (001) Schottky junctions. *Phys. Rev. B*, 79:073101, 2009.

[22] J. M. D. Coey. Magnetism and magnetic materials. Cambridge University Press, 2009.

[23] R. C. O'Handley. Modern magnetic materials. John Wiley and Sons, Inc., 2000.

[24] M. Farle. Ferromagnetic resonance of ultrathin metallic layers. *Reports Prog. Phys.*, 61:755–826, 1998.

[25] A. Aharoni. Demagnetizing factors for rectangular ferromagnetic prisms. *J. Appl. Phys.*, 83:3432, 1998.

[26] M. T. Johnson, P. J. H. Bloemen, F. J. A. den Broeder, and J. J. de Vries. Magnetic anisotropy in metallic multilayers. *Rep. Prog. Phys.*, 59:1409–1458, 1996.

[27] I. Barsukov, P. Landeros, R. Meckenstock, J. Lindner, D. Spoddig, Z.-A. Li, B. Krumme, H. Wende, D. L. Mills, and M. Farle. Tuning magnetic relaxation by oblique deposition. *Phys. Rev. B*, 85:014420, 2012.

[28] S. V. Vonsovskii. Ferromagnetic resonance. Pergamon, Oxford, 1960.

[29] I. Harward, T. O'Keevan, A. Hutchison, V. Zagorodnii, and Z. Celinski. A broadband ferromagnetic resonance spectrometer to measure thin films up to 70 GHz. *Rev. Sci. Instrum.*, 82:095115, 2011.

[30] A. M. Goncalves, I. Barsukov, Y.-J. Chen, L. Yang, J. A. Katine, and I. N. Krivorotov. Spin torque ferromagnetic resonance with magnetic field modulation. *Appl. Phys. Lett.*, 103:172406, 2013.

[31] J. Coonrod and B. Rautio. Comparing microstrip and CPW performance. *Microwave Journal*, 55:74–80, 2012.

[32] B. Rosas. The design and test of broadband launches up to 50 GHz on thin and thick substrates. Technical Report, Southwest Microwave, Inc., 2011, available at http://mpd.southwestmicrowave.com/resources/.

[33] M. Harder, Z. X. Cao, Y. S. Gui, X. L. Fan, and C.-M. Hu. Analysis of the line shape of electrically detected ferromagnetic resonance. *Phys. Rev. B*, 84:054423, 2011.

[34] Kh. Zakeri, J. Lindner, I. Barsukov, R. Meckenstock, M. Farle, U. von Hörsten, H. Wende, W. Keune, J. Rocker, S. S. Kalarickal, K. Lenz, W. Kuch, K. Baberschke, and Z. Frait. Spin dynamics in ferromagnets: Gilbert damping and two-magnon scattering. *Phys. Rev. B*, 76:104416, 2007.

[35] R. Arias and D. L. Mills. Extrinsic contributions to the ferromagnetic resonance response of ultrathin films. *Phys. Rev. B*, 60:7395–7409, 1999.

[36] E. Saitoh, M. Ueda, H. Miyajima, and G. Tatara. Conversion of spin current into charge current at room temperature: inverse spin-Hall effect. *Appl. Phys. Lett.*, 88:182509, 2006.

[37] K. Ando, S. Takahashi, J. Ieda, Y. Kajiwara, H. Nakayama, T. Yoshino, K. Harii, Y. Fujikawa, M. Matsuo, S. Maekawa, and E. Saitoh. Inverse spin-Hall effect induced by spin pumping in metallic system. *J. Appl. Phys.*, 109:103913, 2011.

[38] O. Mosendz, J. E. Pearson, F. Y. Fradin, G. E. W. Bauer, S. D. Bader, and A. Hoffmann. Quantifying spin Hall angles from spin pumping: experiments and theory. *Phys. Rev. Lett.*, 104:046601, 2010.

[39] M.-H. Nguyen, D. C. Ralph, and R.A. Buhrman. Spin torque study of the spin Hall conductivity and spin diffusion length in platinum thin films with varying resistivity. *Phys. Rev. Lett.*, 116:126601, 2016.

[40] S. Takahashi and S. Maekawa. Spin current, spin accumulation and spin Hall effect. *Sci. Technol. Adv. Mater.*, 9:014105, 2008.

[41] M. Weiler, J. M. Shaw, H. T. Nembach, and T. J. Silva. Phase-sensitive detection of spin pumping via the ac inverse spin Hall effect. *Phys. Rev. Lett.*, 113:157204, 2014.

[42] M. I. Dyakonov and V. I. Perel. Current-induced spin orientation of electrons in semiconductors. *Phys. Lett. A*, 35:459, 1971.

[43] J. E. Hirsch. Spin Hall Effect. *Phys. Rev. Lett.*, 83:1834, 1999.

[44] M. Harder, Y. S. Gui, and C.-M. Hu. Electrical detection of magnetization dynamics via spin rectification effects. *Phys. Rep.*, 661:1–59, 2016.

[45] Z. Duan, C. T. Boone, X. Cheng, I. N. Krivorotov, N. Reckers, S. Stienen, M. Farle, and J. Lindner. Spin-wave modes in permalloy/platinum wires and tuning of the mode damping by spin Hall current. *Phys. Rev. B*, 90:024427, 2014.

[46] M. Bailleul. Shielding of the electromagnetic field of a coplanar waveguide by a metal film: Implications for broadband ferromagnetic resonance measurements. *Appl. Phys. Lett.*, 103:192405, 2013.

[47] M. Kostylev. Strong asymmetry of microwave absorption by bilayer conducting ferromagnetic films in the microstrip-line based broadband ferromagnetic resonance. *J. Appl. Phys.*, 106:043903, 2009.

[48] G. Y. Luo, M. Belmeguenai, Y. Roussigné, C. R. Chang, J. G. Lin, and S. M. Chérif. Enhanced magnetic damping in $La_{0.7}Sr_{0.3}MnO_3$ capped by normal metal layer. *AIP Adv.*, 5:097148, 2015.

[49] V. A. Ivanshin, J. Deisenhofer, H.-A. Krug von Nidda, A. Loidl, A. A. Mukhin, A. M. Balbashov, and M. V. Eremin. ESR study in lightly doped $La_{1-x}Sr_xMnO_3$. *Phys. Rev. B*, 61:6213–6219, 2000.

[50] Å. Monsen, J. E. Boschker, F. Macià, J. W. Wells, P. Nordblad, A. D. Kent, R. Mathieu, T. Tybell, and E. Wahlström. Thickness dependence of dynamic and static magnetic properties of pulsed laser deposited $La_{0.7}Sr_{0.3}MnO_3$ films on SrTiO3(001). *J. Magn. Magn. Mater.*, 369:197–204, 2014.

[51] M. Belmeguenai, S. Mercone, C. Adamo, T. Chauveau, L.. Méchin, P. Monod, P. Moch, and D. G. Schlom. $La_{0.7}Sr_{0.3}MnO_3$ thin films on $SrTiO_3$ and $CaTiO_3$ buffered Si substrates: structural, static, and dynamic magnetic properties. *J. Nanoparticle Res.*, 13:5669–5675, 2011.

[52] M. Mathews, F. M. Postma, J. C. Lodder, R. Jansen, G. Rijnders, and D. H. A. Blank. Step-induced uniaxial magnetic anisotropy of $La_{0.67}Sr_{0.33}MnO_3$ thin films. *Appl. Phys. Lett.*, 87:242507, 2005.

[53] P. Perna, C. Rodrigo, E. Jimenez, F. J. Teran, N. Mikuszeit, L. Mechin, J. Camarero, and R. Miranda. Tailoring magnetic anisotropy in epitaxial half metallic $La_{0.7}Sr_{0.3}MnO_3$ thin films. *J. Appl. Phys.*, 110:013919, 2011.

[54] I. Barsukov, R. Meckenstock, J. Lindner, M. Moller, C. Hassel, O. Posth, M. Farle, and H. Wende. Tailoring spin relaxation in thin films by tuning extrinsic relaxation channels. *IEEE Trans. Magn.*, 46:2252–2255, 2010.

[55] G. Counil, J.-V. Kim, T. Devolder, C. Chappert, K. Shigeto, and Y. Otani. Spin wave contributions to the high-frequency magnetic response of thin films obtained with inductive methods. *J. Appl. Phys.*, 95:5646, 2004.

[56] H. T. Nembach, T. J. Silva, J. M. Shaw, M. L. Schneider, M. J. Carey, S. Maat, and J. R. Childress. Perpendicular ferromagnetic resonance measurements of damping and Lande ġ- factor in sputtered $(Co_2Mn)_{1-x}Ge_x$ thin films. *Phys. Rev. B*, 84:054424, 2011.

[57] J. Lindner, I. Barsukov, C. Raeder, C. Hassel, O. Posth, R. Meckenstock, P. Landeros, and D. L. Mills. Two-magnon damping in thin films in case of canted magnetization: Theory versus experiment. *Phys. Rev. B*, 80:224421, 2009.

[58] G. Y. Luo, C. R. Chang, and J. G. Lin. Thickness dependent spin pumping effects in $La_{0.7}$ $Sr_{0.3}MnO_3$/Platinum bilayer film. *IEEE Trans. Magn.*, 49:4371–4374, 2013.

[59] I. Barsukov, S. Mankovsky, A. Rubacheva, R. Meckenstock, D. Spoddig, J. Lindner, N. Melnichak, B. Krumme, S. I. Makarov, H. Wende, H. Ebert, and M. Farle. Magnetocrystalline anisotropy and Gilbert damping in iron-rich $Fe_{1-x}Si_x$ thin films. *Phys. Rev. B*, 84:180405, 2011.

[60] C. Scheck, L. Cheng, I. Barsukov, Z. Frait, and W. E. Bailey. Low relaxation rate in epitaxial vanadium-doped ultrathin iron films. *Phys. Rev. Lett.*, 98:117601, 2007.

[61] S. Mizukami, D. Watanabe, M. Oogane, Y. Ando, Y. Miura, M. Shirai, and T. Miyazaki. Low damping constant for Co_3FeAl Heusler alloy films and its correlation with density of states. *J. Appl. Phys.*, 105:07D306, 2009.

[62] R. A. Gallardo, A. Banholzer, K. Wagner, M Körner, K. Lenz, M. Farle, J. Lindner, J. Fassbender, and P. Landeros. Splitting of spin-wave modes in thin films with arrays of periodic perturbations: theory and experiment. *New J. Phys.*, 16:023015, 2014.

[63] S. I. Kiselev, J. C. Sankey, I. N. Krivorotov, N. C. Emley, R. J. Schoelkopf, R. A. Buhrman, and D. C. Ralph. Microwave oscillations of a nanomagnet driven by a spin-polarized current. *Nature*, 425:380–383, 2003.

[64] L. Yang, R. Verba, V. Tiberkevich, T. Schneider, A. Smith, Z. Duan, B. Youngblood, K. Lenz, J. Lindner, A. N. Slavin, and I. N. Krivorotov. Reduction of phase noise in nanowire spin orbit torque oscillators. *Sci. Rep.*, 5:16942, 2015.